High-MgO lavas associated to CFB as indicators of plume-related thermochemical effects: the case of ultra-titaniferous picrite-basalt from the Northern Ethiopian-Yemeni Plateau

Claudio Natali[1], Luigi Beccaluva[1], Gianluca Bianchini G.[1], Robert M. Ellam[2], Andrea Savo[1], Franca Siena[1], Finlay M. Stuart[2]

[1] Department of Physics and Earth Sciences, University of Ferrara, via Saragat 1, 44121 Ferrara - Italy

[2] Scottish Universities Environmental Research Centre, East Kilbride, G75 0QF - UK

Abstract

A comprehensive petrological and geochemical dataset is reported in order to define the thermo-compositional characteristics of Ti (Fe)-enriched picrite-basalt lavas (HT2, TiO_2 3-7 wt%), erupted close to the axial zone of the inferred Afar mantle plume, at the centre of the originally continuous Ethiopian-Yemeni CFB plateau (ca. 30Ma) which is zonally arranged with progressively lower Ti basalts (HT1, TiO_2 2-4 wt%; LT, TiO_2 1-3 wt%) toward the periphery. Integrated petrogenetic modelling based on major and trace element analyses of bulk rocks, minerals and melt inclusions in olivines, as well as Sr-Nd-Pb-He-O isotope compositional variations enables us to make several conclusions. 1) The phase equilibria constraints indicate that HT2 primary picrites were generated at ca. 1570°C mantle potential temperatures (T_p) in the pressure range 4-5 GPa whereas the HT1 and LT primary melts formed at shallower level (<2 to 3 GPa, T_p 1530 °C for HT1 and 1430°C for LT). Thus the Afar plume head was a thermally and compositionally zoned melting region with maximum excess temperatures of 300-350°C with respect to the ambient mantle. 2) The HT2 primary melts upwelled nearly adiabatically to the base of the continental crust (ca. 1 GPa) where

fractionation of olivine, followed by clinopyroxene, led to variably differentiated picritic and basaltic magmas. 3) Trace element modelling requires that the primary HT2 melts were generated - either by fractional or batch melting (F 9-10%) - from a mixed garnet peridotite source (85%) with 15% eclogite (derived from transitional MORB protoliths included in Panafrican terranes) that has to be considered a specific Ti-Fe and incompatible element enriched component entrained by the Afar plume. 4) The LT, HT1 and HT2 lavas have $^{143}Nd/^{144}Nd$ = 0.5131-0.5128, whereas Sr-Pb isotopes are positively correlated with TiO_2, varying from $^{87}Sr/^{86}Sr$ 0.7032 and $^{206}Pb/^{204}Pb$ 18.2 in LT basalts to $^{87}Sr/^{86}Sr$ 0.7044 and $^{206}Pb/^{204}Pb$ 19.4 in HT2 picrite-basalts. High $^{3}He/^{4}He$ (15-20 R_A) ratios are exclusively observed in HT2 lavas, confirming earlier evidence that these magmas require a component of deep mantle in addition to eclogite, while the LT basalts may more effectively reflect the signature of the pre-existing mantle domains. The comparison between high-MgO (13-22%) lavas from several Phanerozoic CFB provinces (Karoo, Paranà-Etendeka, Emeishan, Siberia, Deccan, North Atlantic Province) shows that they share extremely high mantle potential temperatures (T_p 1550-1700°C) supporting the view that hot mantle plumes are favoured candidates for triggering many LIPs. However, the high incompatible element and isotopic variability of these high-MgO lavas (and associated CFB) suggest that plume thermal anomalies are not necessarily accompanied by significant and specific chemical effects, which depend on the nature of mantle materials recycled during the plume rise, as well as by the extent of related mantle enrichments (if any) on the pre-existing lithospheric section.

1. Introduction

There is a longstanding debate on the generation of Large Igneous Province (LIP), either attributed to mantle plumes, melting anomalies in compositionally heterogeneous mantle (see Special Papers by Ernst and Buckan, 2001a; Foulger et al., 2005, Foulger and Jurdy, 2007; Beccaluva et al., 2011a) or even to mantle warming beneath continents (Coltice et al., 2009)~~,~~.

A great contribution to the plume debate has been provided by the tracking through the geological time (from Archean to Phanerozoic) of large amounts of erupted magmas emplaced in a short time in both continental and oceanic settings (Ernst and Buckan, 2001b; Courtillot et al., 2003; Safonova and Santosh, 2014; Reichow et al., 2009). Among the various magma types observed in LIPs, an increasing interest has been devoted to high-Mg lavas that–owing to their primitiveness, deep-seated origin and general lack of crustal contamination could be considered effective proxies for plume-related magmas.

High-Mg lavas such as picritic basalts, (ferro)picrites and meimechites, are observed in many Phanerozoic LIP where they represent minor but significant components in both continental and oceanic flood basalt sequences (Karoo, Deccan, Siberia, Ethiopia-Yemen, Paranà-Etendeka, North Atlantic Province-NAP, Emeishan and Caribbean). The intrinsic characteristics of high-Mg magmas led many authors to consider them as the deepest and hottest melting products of an upwelling mantle plume (Ellam and Cox, 1991; Ellam et al., 1992; Thomson et al., 2001; Herzberg and O'Hara, 2002; Campbell and Davis, 2006; Carlson et al., 2006; Beccaluva et al., 2009; Zhang et al., 2010), thus more effectively recording its thermo-chemical effects with respect to the associated basalts. Accordingly, some compositional features of these high-Mg magmas -such as low-Al, high-Fe, variable Ti and Ocean Island Basalt (OIB)-like trace element and isotopic signatures- have been considered indicative of generation at high P-T conditions with the involvement of pyroxenite/eclogite components in their mantle sources (Gibson et al., 2000; Beccaluva et al., 2009; Sobolev et al., 2007 and 2009; Buslov et al., 2010; Kamenetskey et al., 2012; Heinonen et al., 2013 and 2014).

Application of olivine-melt equilibria constraints in high-Mg lavas, generally allows reliable evaluations of olivine cumulus/fractionation processes as well as reconstruction of primary magmas and the relative mantle potential temperatures (Herzberg et al., 2007). On the other hand, there are several aspects that need additional investigations, in particular, the

significance of picrites with respect to the compositional variability and zonation of the associated basalts (Low-Ti, High-Ti) as well as their mutual spatial/temporal relationships which are often unclear. In general, there is a need for a better understanding of the role of high-Mg magmas in the whole thermo-compositional and spatial development of a LIP and, by implication, the causative events of thermal anomalies in the mantle.

In this context, the 30 Ma Northern Ethiopian-Yemeni LIP is of particular interest as it consists of a large originally continuous CFB plateau, characterized by zonal arrangement with picritic-basaltic lavas at the centre corresponding to the Afar triple junction which is considered the axis of a deep mantle plume active beneath the Afro-Arabian region during Oligocene (Beccaluva et al., 2009; Natali et al., 2011; Rooney et al., 2012). This picrite-basalt association includes the most Ti enriched high-Mg lavas so far observed in CFB sequences (TiO_2 up to 7 wt%), comparable only with meimechites from the Siberian Traps (Carlson et al., 2006; Sobolev et al., 2009). Their peculiar composition together with their position at the core of the Oligocene CFB plateau make these rocks extremely interesting to evaluate both the temperature of the Afar mantle plume at the time of CFB eruption and its contribution to the composition of the related. Moreover, systematic investigations on mantle xenoliths included in Neogene alkaline lavas overlying the CFB plateau, and from neighbouring districts, now provide direct insights on the nature of the ambient mantle and allow important constraints to be placed on the primary melt petrogenesis in the Afro-Arabian domain (Beccaluva et al., 2011b; Bianchini et al, 2014; Sgualdo et al., 2015).

In this work we present new data including major and trace element analyses on bulk rock, constituent minerals and melt inclusions, as well as Sr-Nd-Pb-He-O isotopes, that are used to constrain: 1) the petrogenesis of picritic melts in terms of physico-chemical conditions and melting regime; 2) the significance of picrite-basalts in the CFB zonal arrangement and 3) the definition of the nature and role of the Afar plume components compared with those of other LIP.

2. Geological setting

The Northern Ethiopian-Yemeni CFB province represents a LIP widely considered to be related to the activity of the Afar plume, on the basis of geophysical, geochemical and volcanotectonic features. (Hoffmann et al., 1997, Ebinger and Sleep, 1998; Pik et al., 1999 and 2006, Davaille et al., 2005; Rogers, 2006; Yirgu et al., 2006; Beccaluva et al., 2009, Bastow et al., 2011; Chang and Van der Lee, 2011; Moucha and Forte, 2011; Natali et al., 2011 and 2013). The impinging of this plume on the Afro-Arabian domain, at least since the Late Eocene, caused up to ca. 3 km regional uplift and doming of the lithosphere (Sengor, 2001; Gani et al., 2007) accompanied by extension and faulting that favoured rapid CFB ascent and eruption. Geophysical data indicate a present day lithosphere thickness of 80-90 km, including 35-40 km of continental crust that is variously underplated by basic intrusions (Bastow et al., 2008 and 2011).

Ethiopian-Yemeni CFB were erupted at ca. 30 Ma (Baker et al., 1996; Hoffmann et al., 1997; Ukstins et al., 2002) as a subcircular (700 km in diameter) originally continuous plateau covering an area of ca. 400,000 km^2. The basaltic plateau is almost entirely composed by lava flows, (occasionally including dyke swarms; Mège and Korme, 2004), and overlies Mesozoic sedimentary units or the Pan-African crystalline basement (Beccaluva et al., 2009 and references therein). It was subsequently dismembered by the Red Sea/Afar opening (Bellahsen et al., 2003, Bosworth et al., 2005) and is now represented by the uplifted relic portions of the northern Ethiopian and the Yemeni plateaus at the Africa/Arabia conjugate margins (Fig. 1). Restoration of the Yemeni plateau to its original configuration confirms the zonal arrangement of CFB lavas which are represented by 1) low-Ti (LT) tholeiites in the north-western periphery, 2) high-Ti tholeiites (HT1) in the intermediate position and 3) very high-Ti transitional basalts and picrites (HT2) –interbedded with minor HT1 lavas and locally topped by rhyolitic differentiates– near the centre of the subcircular plateau area (Beccaluva

et al., 2009; 2011b; Natali et al., 2011). The HT2 lavas, erupted at the inferred Afar plume axis are concentrated in the Lalibela district (Northern Ethiopia) where the volcanic pile is ca. 2 km thick and in the Manakhah section at the northernmost portion of the Yemeni plateau, where the maximum thickness is ca. 1 km. GIS-based reconstruction of the HT2 basalt and picrite lavas accounts for ca. 50,000 km^3, covering a subcircular area of ca. 200 km diameter, that corresponds to 16% of the whole CFB volume (ca. 310,000 km^3). Given the short time span of activity (≤ 1Ma; Hofmann, 1997) this implies an eruption rate of ca. 0.3 km^3 per year for Northern Ethiopia-Yemeni plateau, which is comparable to that of other CFB provinces (Farmer, 2003).

3. Materials and methods

Sampling has been based on several field works in 2004, 2006, 2009 and 2012 for the Ethiopian plateau and on a field trip organized by the Yemeni Geological Survey in 2007 for the Yemeni counterpart. In particular, HT2 picrite-basalt lavas were mainly collected from the two sections of Manakhah (Northern Yemeni plateau) and Lalibela (Northern Ethiopian plateau). Latitude and longitude of the sampling locations (Table 1) were used for GIS-based reconstructions of the 3D geometry of distinct magmatic groups (LT, HT1 and HT2) carried out using topographic information from NASA SRTM images and applying polynomial interpolations.

With regards to the geochemical investigation, the least altered and most representative volcanic lithotypes were selected out of 70 specimens and powdered in an agate mill. Major and trace elements (Ni, Co, Cr, V, Sc, Rb, Sr, Ba and Zr) were analysed by X-ray fluorescence (XRF) on powder pellets, using a wavelength-dispersive automated ARL Advant'X spectrometer at the Department of Earth Sciences, Ferrara University. Accuracy and precision for major elements are estimated as better than 3% for Si, Ti, Fe, Ca and K, and 7% for Mg, Al, Mn, Na; for trace elements (above 10 ppm) they are better than 10%. REE, Y,

Hf, Nb, Th, and U were analysed by inductively coupled mass spectrometry (ICP-MS) at the Department of Earth Sciences, Ferrara University, using a Thermo-Scientific X-Series. Accuracy and precision, based on the replicated analyses of samples and standards, are estimated as better than 10% for all elements, well above the detection limit.

Mineral compositions were obtained at the CNR-IGG Institute of Padova with a Cameca SX-50 electron microprobe (fitted with three wavelength dispersive spectrometers) at an accelerating voltage of 15 kV, and specimen current of 20 nA, using natural silicates and oxides as standards; the analysis of glasses and hydrous mineral phases required a distinct analytical setting and the beam current was lowered to 2 nA in order to mitigate the loss of alkali and halogens. Trace element analyses of constituent mineral phases were carried out at the CNR-IGG of Pavia by laser ablation microanalysis (LAM) ICP-MS, using an Elan DRC-e mass spectrometer coupled with a Q-switched Nd:YAG laser source (Quantel Brilliant). The CaO content was used as an internal standard. Precision and accuracy, better than 10% for concentrations at ppm level, were assessed by repeated analyses of NIST SRM 612 and BCR-2 standards.

Sr-Nd-Pb isotopic analyses on bulk rock and handpicked clinopyroxene (~200 mg) were carried out mainly at SUERC (Scottish Universities Environmental Research Centre). Samples were digested with a mixture of HF-HNO_3-HCl and prepared as described by Hardarson et al. (1997). Sr and Nd isotopes were analyzed using a VG Sector 54-30 mass spectrometer in multidynamic mode using exponential corrections for mass fractionation and $^{86}Sr/^{88}Sr = 0.1194$, $^{144}Nd/^{146}Nd = 0.7219$. Within the period, the NBS 987 standard gave a $^{87}Sr/^{86}Sr$ value of 0.710247 (2σ 0.000021, n=18) and the internal laboratory J&M standard gave a $^{143}Nd/^{144}Nd$ value of 0.511515 (2σ 0.000022, n=23). Pb isotopes were analyzed using a Micromass IsoProbe multicollector ICP-MS. Pb was measured using a method similar to that described by Ellam (2006). Mass fractionation was corrected according to the Tl-doping method by adding NIST997 Tl to produce solutions for analysis with 50ng/g Pb and 5 ng/g

Pb. The correction was made using an an exponential law and $^{205}Tl/^{203}Tl$=2.3871. NBS 981 gave $^{206}Pb/^{204}Pb$ = 16.937±4, $^{207}Pb/^{204}Pb$ = 15.498±5, and $^{208}Pb/^{204}Pb$ = 36.720±17 (2σ, n=11). A subordinate subset of Sr-Nd-Pb analyses was carried out at the CNR-IGG of Pisa, where Sr-Nd-Pb isotopic compositions were determined by a Finnigan MAT 262 multi-collector mass-spectrometer following the methods described in Saccani et al. (2013) and Del Moro et al. (2015). In this laboratory replicate analyses of the NBS 987 standard gave an average $^{86}Sr/^{88}Sr$ value of 0.710253±13 (2σ, n=30), whereas the isotopic standard JNdi-1 (Tanaka et al., 2000) gave an average $^{143}Nd/^{144}Nd$ value of 0.512098±8 (2σ, n=25). As concern Pb, replicate analyses are accurate to within 0.025% (2σ) per mass unit, after applying mass discrimination correction of 0.15±0.01 per mass unit relative to the NBS 981 reference composition of Todt et al. (1993).

Olivine separates for helium isotope analysis were picked under a binocular microscope and washed ultrasonically in HNO_3 and then water, prior to a final treatment with analar acetone. Helium was extracted from all minerals by in vacuo crushing and analyzed using a MAP 215-50 mass spectrometer at SUERC using procedures slightly modified from Stuart et al. (2000).

Oxygen isotopic compositions of mineral separates were measured at the CNR–IGG Institute of Pisa by conventional laser fluorination (Sharp, 1995). To measure the oxygen isotopic composition of each phase, 1–1.5 mg crystals were taken and laser fluorinated with a 25W CO_2 laser, at a wavelength of 10.6 μm. Pure fluorine desorbed at 290–310°C from hexafluoropotassium-nickelate salt (Asprey, 1976) was used as reagent. The O_2 produced during laser fluorination was purified from excess fluorine by means of a KCl trap held at 180°C, and the chlorine was trapped cryogenically. The gas was then transferred to a 13Å molecular sieve-filled cold finger and analysed for its oxygen isotopic composition using a Finnigan Delta Plus mass spectrometer. Each day of analysis, normally 4–7 aliquots of internal laboratory quartz standards were analysed, with an average reproducibility of ±0.14

% (1σ). Samples were analysed twice, with an analytical precision of ±0.2 % (1σ) or better. No data correction was necessary for the results, which are reported in the standard $\delta^{18}O$ notation (‰, relative to V-SMOW).

4. Bulk rock, mineral and melt inclusion chemistry

Major and trace element analyses of the investigated HT2 lavas are reported in Table 1, whereas data on their constituent minerals and melt inclusions in olivine, as well as interstitial glasses are reported in Supplementary Table 1 and Table 2, respectively.

HT2 basalts and picrites from the Lalibela and Manakhah sequences are always porphyritic in texture with phenocrysts (up to 5 mm across) of olivine, sometimes including Cr-spinel, pinkish clinopyroxene and rare plagioclase; the groundmass is microcrystalline to hypocrystalline (particularly in picrites) and is made up of the same phases with the addition of Fe–Ti oxides, scarce phlogopite (and sporadic kaersutite), alkali feldspar, apatite and interstitial glass. While Ethiopian lavas are generally fresh, Yemeni rocks variably contain secondary minerals mainly represented by serpentine on olivine and infilling carbonates, as indicated by the relatively high Loss On Ignition (LOI, Table 1). The main petrographic difference between picrites and basalts is the prevalence of olivine phenocrysts (up to 20-25%) over clinopyroxene in the former, whereas the reverse is observed in basalts. For classification purposes, picrites can be chemically distinguished from basalts on the basis of their higher MgO (> 13 wt%) and Ni (> 500 ppm) contents. In the Total Alkali-Silica (TAS) diagram of Fig. 2 the HT2 rocks cluster around the alkaline/subalkaline boundary displaying a more alkaline transitional character with respect to LT and HT1 basalts, which mostly plot in the subalkaline field. Within the HT2 group, Yemeni lavas display a more alkaline character with respect to Ethiopian analogues. This cannot be merely ascribed to alteration processes, as the increase of alkalinity in Yemeni lavas is reflected by systematic higher Na_2O/K_2O ratios (3.5 and 1.9 on average for Yemeni and Ethiopian lavas, respectively) as

well as by the clinopyroxene chemistry discussed below. Some relevant intergroup compositional variations are shown in the binary diagrams of Fig. 3 where empirical boundaries discriminate between LT, HT1 and HT2 lavas. The remarkable progressive increase of TiO_2, Nb and Ce from LT to HT2 in a direction nearly orthogonal to the boundaries, cannot be explained only by variation of degree and P-T conditions of melting but necessarily implies specific enrichment for the respective magma sources. Although less evident, a parallel iron enrichment is observed particularly in HT2 lavas indicating that source variation also involved major element components and were zonally arranged in the Ethiopian-Yemeni plateau (Beccaluva et al., 2009). On the other hand, intra-group variations related to common fractionation processes are shown the by negative correlation between MgO and FeOt, TiO_2, Nb and Ce. Although occasional crustal contamination can not be excluded as proposed by Pik et al. (1999), particularly for LT magmas, the coherence of the observed trends seems to preclude a major role of this process in the samples considered in this study.

Mineral composition in the picrite/basalt suite shows slight but significant variations (Supplementary Table 1a-e). Olivine in picrites and basalts share the same compositional range (Fo from 76.5 to 90.4) with crystal cores of picrites clustering between Fo 87.5 and 90.2. NiO in olivines varies from 0.5 to 0.2 wt% and is broadly correlated with the Fo content; CaO is in the range 0.2-0.4 wt% (average 0.3 wt%), comparable with that of olivines in high-MgO lavas from other CFB provinces (Thompson and Gibson, 2000). Clinopyroxene is generally augite in the Lalibela picrites and basalts, whereas it shows a diopside tendency in the Manakhah lavas, reflecting the more alkaline character of the Yemeni rocks. Groundmass plagioclase varies between An62 and An40 and is coupled with minor alkali feldspar (Or up to 53.4), scarce Ti-rich phlogopite (TiO_2 up to 9.5 wt%) and sporadic kaersutite (TiO_2 up to 7.6 wt%). Cr-Fe-Ti oxides are represented by Cr-spinel included in olivine phenocrysts and Ti-magnetite/ilmenite in the groundmass. Cr- spinel (Cr# 0.81-0.65)

displays a particularly high TiO_2 content (up to 10.6 wt%) comparable to some other CFB picritic rocks (Desta et al., 2014 and references therein). Groundmass Ti-magnetite shows ülvospinel content varying from 34 to 56% and is always coupled with ilmenite.

Melt inclusions (MI, 20-100 μm in size) in olivine phenocrysts were analyzed in two picrites (LAL70, LAL73) and one basalt (LAL42) from Lalibela (Table 2). Although showing a wide compositional range (MgO 3.3-15.4 wt%) they invariably display high TiO_2 content (2.3-5.4 wt%). In the TAS diagram of Fig. 2 MI vary in composition from picrite to basaltic andesite, mostly overlapping the picrite-basalt bulk rock distribution. The analysis of MI-LAL70, corrected for post-entrapment olivine crystallization (Danyushevsky et al., 2002), shows a picritic composition (MgO = 15.4 wt%) and displays a slightly more alkaline character compared to HT2 Ethiopian bulk rocks. Analyses of MI-LAL73 and MI-LAL42 show a variable composition in the basaltic field, which reflects trapping of cogenetic melt fractions at various differentiation stages. It is noteworthy that groundmass interstitial glasses from picrite LAL73 (Table 2) expand the MI fractionation trend toward an andesitic composition, thus recording a wide magmatic evolution even in the same sample.

The trace element characteristics of Northern Ethiopia-Yemeni HT2 picrite-basalt lavas are illustrated in the Chondrite (Ch)-normalized and Primordial Mantle (PM)-normalized diagrams of Fig. 4. The Rare Earth Elements (REE) distribution invariably shows a continuous positively fractionated pattern with remarkable Light (L)REE enrichment (La_N/Yb_N from 8 to 18; Tb_N/Yb_N 2.7-3.8). Although subparallel and largely overlapped, the lowest and the highest REE levels are recorded by some picrites and basalts, respectively (Fig. 4a). In Fig. 4b the PM-normalized incompatible element distribution of HT2 lavas generally shows upward-convex patterns that conform to those of transitional/alkaline Ocean Island Basalt (OIB) from within-plate setting (Sun and McDonough, 1989; Hoffmann, 1997), and, particularly to the EM2-types (Weaver et al., 1991). However, these spiderdiagrams

reveal that most HT2 rocks are enriched in Ti and more in general in High Field Strength Elements (HFSE) such as Zr and Nb.

The incompatible element distribution of MI satisfactorily matches the picrite-basalt bulk-rock field, with sample MI-LAL70 approaching the most primary picritic compositions, whereas the other MI and the interstitial glass depict variably enriched patterns which reflect the fractionation degree (Fig 4c). Trace element analyses of clinopyroxene in the picrite-basalt association are reported in Table 3 and in the Ch-normalized diagram of Fig. 5. The observed upward-convex patterns (La_N/Yb_N 1.0-4.4, Sm_N/Yb_N 3.3-10.6) resemble those from alkaline basalts (Jeffries et al., 1995), in agreement with the transitional to alkaline character of the relative magmas, which is even more emphasized in the Yemeni rocks. The HREE fractionation (Tb_N/Yb_N 2.1-6.0) of these clinopyroxenes mimics those of the relative bulk rocks. Similar clinopyroxene patterns have been also observed in High-MgO plume-related magmas from other LIPs (Kamentesky et al. 2012; Wei et al., 2015) and interpreted as a garnet signature in the magma sources. Interestingly, significant clinopyroxene compositional variations (e.g. height of the pattern) are often observed within the same rock sample, possibly as a result of either polybaric fractionation or mixing/cumulus processes.

5. Petrogenesis of the picrite-basalt association

The identification of primary and parental magmas of a suite is not straightforward even when dealing with high-MgO lavas, not only because of the difficulty of estimating thermobarometric conditions, melting regime and source composition, but also due to mixing and cumulus processes affecting magmas rising in a short time along the same feeding system, as is the case of the investigated picrite-basalt association. The integration of multiple approaches, such as major element phase equilibria and trace element modelling, may help to put constraints on primitiveness of magmas and P-T-X conditions of their mantle sources as discussed below.

5.1 The quest for primary and parental melts

Most picrites of the studied HT2 association have mg# between 0.68 and 0.72, thus showing potential equilibrium with a mantle source with olivine Fo>0.88 (Herzberg and O'Hara, 2002, Green and Falloon, 2005). Stronger constraints are provided by the MgO-FeO diagram (Fig. 6, modified after Herzberg et al., 2007), where the petrogenetic grid for primary melts and fractionation trends of OIB, plateau basalts and MORB suites are reported, together with Fo composition arrays of coexisting olivine. In this diagram, the Ethiopian-Yemeni HT2 lavas define a relatively high FeO distribution roughly reflecting various extent of magmatic fractionation from picrites to basalt, as well as significant olivine accumulation in some samples (samples labelled with *c*). Coherently, in Fig. 7, it can be observed that although many samples show an olivine compositional range encompassing the equilibrium conditions with the respective whole rock ($Kd_{Ol\text{-}rock}$ = 0.28-0.32), most of the analyzed olivines show disequilibrium. This is probably due to the intrinsic mechanism of olivine crystallization in picritic magmas, which is characterized by rapid growth and compositional changes, leading to persistent disequilibrium conditions during crystallization. This implies that only a few picritic samples (*i.e.* LAL5, LAL6 and LAL9), displaying restricted olivine compositional ranges in equilibrium ($Fo_{88.8\text{-}90.2}$) with the respective bulk rock (mg# 0.69–0.72), confidently represent suitable parental magmas for petrogenetic modelling Accordingly, the accumulated fractional melting model of Herzberg and Asimow (2015) was applied to these most primitive picrites, assuming Fe^{2+}/Fe_{tot} = 0.9, using as source composition both the notional garnet lherzolite source KR4003 (Walter, 1998) and the average of Ethiopian lherzolite mantle xenoliths (MgO 39.7 wt%, FeO 8.6 wt%; Beccaluva et al., 2011b). In all cases no limit to the model applicability was observed for the selected compositions (see Appendix A in Herzberg and Asimow, 2015)*:* the calculated primary melts have MgO contents in the range 19.8-21.6 wt% and average mantle potential temperatures

nearly coincident either assuming as magma source the Ethiopian xenoliths (T_p 1570°C) or the KR4003 peridotite (T_p 1585 °C). This suggests that, at least in terms of bulk chemical composition, the sub-Ethiopian mantle xenoliths are appropriate for modelling the source of the Ethiopian-Yemeni CFB.

Compared with other high-MgO lavas from various plateau basalts, OIB and MORB settings (Fig. 8), the Ethiopian-Yemeni data overlap those obtained from NAP and Deccan and, together with other CFB provinces (Etendeka, Karoo, Emeishan and Siberia), represent the highest T_p range (1550-1700°C) which characterizes Phanerozoic continental LIP. By contrast, oceanic plateaux, such as Ontong Java and Caribbean, and OIB (Hawaii, Gorgona and Iceland), are generally cooler in a T_p range 1550-1400°C. Application of the above modelling to the most primitive LT and HT1 basalts allows comparison between the peripheral magmas of the Ethiopian-Yemeni plateau with those of its axial zone (HT2 group): the calculated LT and HT1 primary magmas (data from Baker et al., 1996; Beccaluva et al., 2009; Teklay et al., 2005 and unpublished author data) have 14 and 18 wt% MgO, respectively (Fig. 6). The corresponding T_p are 1430°C for LT, and 1530°C for HT1 which indicates that the Ethiopian-Yemeni CFB are clearly zoned both compositionally and thermally ($\Delta T_{p\max}$ 140°C). Overall, in spite of the limits of the applied model for the T_p estimate (see discussion by Heinonen et al., 2015), the obtained data are reasonably consistent both for the internal comparison within Ethiopian-Yemeni CFB and with other LIP occurrences worldwide. Noteworthy, alternative thermometric estimates (such as Al-in-olivine thermometer, Coogan et al., 2014), although giving systematically lower temperatures (ca. 100°C), do not obscure the presence and extent of LIP-related thermal anomalies (Heinonen et al., 2015).

Phase equilibria constraints, according to Herzberg et al. (2007), indicate that the calculated primary HT2 picrites correspond to a melt fraction in the range 0.10-0.15 generated by a garnet-bearing peridotite mantle source at 4-5 GPa pressure. The application

of the Gudfinnsson and Presnall (2005) and Herzberg and Zhang (1996) whole rock geobarometers confirm the above pressure range of melting. On the other hand, the same parameterization indicates that LT and HT1 primary magmas could be generated by 0.15-0.25 melt fraction of a spinel peridotite in the pressure range < 2 to 3 GPa, which extends the previous estimates for LT and HT1 generation to higher pressure (1.3-2.2 GPa; Beccaluva et al., 2009).

5.2 Modelling the fractionation trends

This section will discuss the application of a forward fractionation model to test the possible derivation of HT2 basalts from the associated picrites. Starting from the calculated primary picrites, fractional crystallization modelling (*Petrolog v.3;* Danyushevsky and Plechov, 2011) indicates that the observed differentiation trends up to the most fractionated basalt (MgO ca. 5 wt%) can be accounted for by relatively low pressure fractionation (Fig. 6 and 8). In fact, high pressure conditions would not fit mineral/rock equilibria, whereas polybaric fractional crystallization starting at pressure $\leq$ 1 GPa can reproduce the compositional variations observed in olivine and particularly clinopyroxene phenocrysts, as well as in the whole rocks. Accordingly, equilibrium olivine starts to crystallize at a temperature of ca. 1510°C (Fo 91.3), implying that primary magmas (T_p 1570°C) upwelled nearly adiabatically to the base of the crust. Crystal fractionation is dominated by olivine up to ca. 1260°C where clinopyroxene (mg# ca. 0.86) join olivine in cotectic crystallization (Fig. 8). The final basaltic composition is attained after removal of a total amount of ca. 50% solid phases (33 % olivine and 17% clinopyroxene).

The above data suggest that the genesis and evolution of the picrite-basalt association reflect a complex T-P-X path, likely starting from the generation of primary picritic melts at high potential temperature and pressure (1570°C, 4-5 GPa), followed by nearly-adiabatic magma rising up to the onset of non-adiabatic regime at crustal level (<1 GPa), where picritic

magmas slowed down and underwent fractional crystallization with formation of variably differentiated magmas. The same modelling has been also applied for LT and HT1 primary melts (data from Baker et al., 1996; Beccaluva et al., 2009; Teklay et al., 2005 and unpublished author data). For LT olivine (Fo 90.3) starts to crystallize at 1420°C, followed by plagioclase (An_{77-81}) at 1200°C, and clinopyroxene (mg# 81-82) at ca. 1160°C. Removal of ca. 60% solid phases (Ol 26%, Pl 26%, Cpx 8%) is required to reach the composition of the most fractionated LT basalt (Fig. 8). Fractionation of HT1 magmas displays intermediate features between LT and HT2 (Fig. 6), with the most fractionated basalt resulting from removal of ca. 50% solid phases (Ol 29%, Cpx 17%, Pl 6%). It is noteworthy that, while the HT2 picrite-basalt evolutionary trend is characterized by the appearance of clinopyroxene crystallization after olivine and a mild Fe-enrichment, conforming to a transitional to alkaline affinity, the LT trend is typically tholeiitic and characterized by extensive plagioclase crystallization after olivine, leading to a marked Fe-enrichment of the evolved magmas (inset of Fig. 6).

Trace element fractional crystallization modelling has also been carried out on the basis of the amount of fractionated solid phases calculated from major elements. Model results reported in PM-normalized incompatible element diagrams of Fig. 9, indicate that there is a good agreement between the computed and the observed differentiated basalts using appropriate partition coefficients (Kd) from GERM database for Ol, Cpx and Pl. It is important to note that nearly identical results are obtained using the clinopyroxene Kd calculated as cpx phenocryst/bulk rock ratios (Table 1 and 3).

5.3 Trace element modelling for the generation of HT2 primary melts

The trace element distributions of the Ethiopia-Yemeni HT2 picrite-basalt are compared in Fig. 10a with other high-Mg lavas from plateau basalts and OIB. Clearly, the differences in incompatible element enrichment among the various provinces are too wide to be accounted

for by olivine cumulus/fractionation processes which commonly affect picritic magmas. Therefore, these differences have to be ascribed to variations in source compositions and/or melting modes. As indicated in the previous section and already suggested by some authors (Kamenetsky et al., 2012; Heinonen & Luttinen, 2008; Gibson et al., 2000), the marked LREE enrichment, the HREE fractionation and the high V/Sc ratios in MgO-rich lavas from most CFB provinces conform to magma originating from deep and variably metasomatized mantle sources with residual garnet. On the other hand, high-Mg lavas from the Caribbean plateau and NAP, together with those from Iceland and Gorgona do not show incompatible element enrichment and HREE fractionation, thus suggesting shallower melting (spinel facies) of their mantle sources (Rèvillon et al., 1999 and 2000).

However, the above considerations are not sufficient to justify the Ti-(Fe) and HFSE (e.g. Zr, Hf) enrichments recorded in CFB lavas such as those from Ethiopia-Yemen, Siberia, Karoo and Emeishan, thus requiring additional components in their mantle sources. The nature of these components could be attributed either to primordial planetary differentiation (Elkins-Tanton et al., 2002; 2011; Solomatov, 2016 and references therein), to plume-related pyroxenite cumulates (Rogers et al., 2010), or to pyroxenite/eclogite material deriving from ancient subducted oceanic slabs subsequently incorporated and melted at high pressure in a rising mantle plume (Siberia, Sobolev et al., 2007 and 2009; Northern Ethiopia, Beccaluva et al., 2009; Karoo, Heinonen et al., 2008). This last hypothesis has gained ground, particularly for explaining the CFB magma genesis. Accordingly, Jennings et al. (2014a; 2014b) observed that the peculiar features of CFB ferropicrites require high P-T_p melting beneath the continental lithosphere that preferentially taps the most fusible eclogite/pyroxenite-rich sublithospheric mantle lithologies.

In this context we extensively reviewed the pyroxenite/eclogite compositions from the literature that should be added to the sub Ethiopian mantle (assumed as lherzolite xenolith GOJ40A; Beccaluva et al., 2011b) in order to obtain a suitable source for the HT2 primary

magmas. Best fit model calculations (Fig. 10b) show that primary picrites could be generated by ca. 10 % of both batch and fractional melting of a mixed garnet lherzolite (85%) and eclogite (15%) source, with the latter corresponding to Neoproterozoic eclogite from Hoggar (Berger et al., 2014). Noteworthy, these eclogites, chemically resembling transitional MORB (cf Le Roex, 1987), record subduction episodes of ancient oceanic lithosphere involved in the Pan-African tectonomagmatic events all along the North African-Arabian domain (Stern and Johnson, 2010). Conceptually, these results can be accommodated in a multi-stage petrogenetic process in which the source is a piclogite domain (Bianchini et al., 2010), resulting from the interaction of pyroxenite/eclogite melt with a garnet peridotite matrix. This implies pyroxenite mobilization, melt generation, upward migration and crystallization, during the incipient rising of the plume head, which is followed by shallower melting of piclogite domains due to further upwelling, with generation of HT2 magmas at 4-5 GPa pressure (*cf* Tuff et al., 2005; Sobolev et al., 2009; Rosenthal et al. 2014). Although simplified for what concern the physical-chemical aspects of the eclogite component mobilization, the trace element modelling allows placing robust constraints on the extent of the peridotite-eclogite hybridization, the degree of melting and the presence of residual garnet in the HT2 mantle source. Moreover, these results are in good agreement with those from major element modelling, as well as with the isotopic data that will be discussed in the next section. Further investigations and modelling on the eclogite/peridotite interaction are beyond the scope of this work and will be the object of future researches.

6. Sr-Nd-Pb-He-O isotope systematics

Sr-Nd-Pb isotopic data of bulk rock and clinopyroxene of the Ethiopian-Yemeni CFB (LT, HT1, HT2) are reported in Table 4. As a whole, the Ethiopian-Yemeni CFB show the following ranges: $^{87}Sr/^{86}Sr$ 0.7032-0.7044 and $^{143}Nd/^{144}Nd$ 0.51274-0.51306, and $^{206}Pb/^{204}Pb$ 18.02-19.41, $^{207}Pb/^{204}Pb$ 15.48-15.63, $^{208}Pb/^{204}Pb$ 37.55-39.46, with the Yemeni rocks having

the higher lead isotopic compositions. Sr-Nd-Pb isotopic data are reported in Fig. 11 and compared with the composition of other flood basalts from major Phanerozoic LIPs. In Fig. 11a the Ethiopian-Yemeni CFB are extremely clustered with $\varepsilon^{(t)}_{Sr}$ between and -18.0 and -2.1, and $\varepsilon^{(t)}_{Nd}$ between +8.3 and +2.3, showing partial overlap with the upper-left portion of CFB fields from Karoo, Deccan and Siberia with the Parana-Etendeka CFB field slightly displaced in the opposite direction. Therefore, very radiogenic Sr and unradiogenic Nd isotopic compositions are lacking in the Ethiopian-Yemeni lavas, implying the absence of the "continental crust" fingerprint envisaged in other CFB provinces. Further comparison is provided by Fig. 11b, where the $^{207}Pb/^{204}Pb$ *vs* $^{206}Pb/^{204}Pb$ composition of Ethiopian-Yemeni lavas is plotted together with data from other Phanerozoic oceanic and continental LIP worldwide (Jackson and Carlson, 2011 and references therein). Here, LT lavas largely overlap those of Baffin Island-West Greenland, Ontong Java Plateau, Deccan and Siberia, whereas HT2 lavas are significantly displaced on the right of the geochrons. According to Jackson and Carlson (2011), this compositional shift could be related to the incorporation of recycled oceanic crust into the non-chondritic Primitive Mantle reservoir, in agreement with the trace element modelling discussed in the previous section.

Differences within the Ethiopia-Yemen CFB are emphasized in Fig. 12 which also includes the notional OIB mantle end-members (DM, EM1, EM2, HIMU; Hofmann, 1997; Stracke et al., 2005). There is a clear covariance between Pb and Sr isotopes, with HT2 lavas showing the more radiogenic values ($^{87}Sr/^{86}Sr$ 0.7040-0.7045, $^{206}Pb/^{204}Pb$ 18.8-19.4, $^{208}Pb/^{204}Pb$ 38.6-39.5), while the Yemeni rocks plot out of the trend due to more radiogenic lead. A covariance is also observed for TiO_2 *vs* $^{87}Sr/^{86}Sr$ and $^{206}Pb/^{204}Pb$, (Fig. 13) with a clear distinction between LT, HT1 and HT2 lava groups. As already seen for the incompatible element distribution, this indicates geochemically distinct mantle sources for LT, HT1 and HT2 lavas, in relation to a progressive enrichment of the titaniferous geochemical component which characterizes the Afar plume. The above correlation (Fig. 13), together with the

relatively restricted range of isotopic data taken as a whole (Fig.11) further precludes the occurrence of significant crustal contamination processes for the samples considered in this study.

For the Yemeni HT2 lavas, the observed differences in lead isotopic composition may be inherited from ancient components in the lithosphere (HIMU?) partially masked (but not reset) by the Afar plume metasomatism. It is noteworthy that these new Sr-Nd-Pb isotopic compositions encompass those of Yemeni flood basalts considered by Baker et al., (1996 and 2000) unaffected by crustal contamination.

Additional information can be obtained comparing the Sr-Nd-Pb isotopic compositions of bulk rock and constituent clinopyroxene, available for a subset of HT2 lavas including both basalts and picrites. The isotopic misfit variously observed in the clinopyroxene-bulk rock pairs, cannot be simply ascribed to differential radiogenic ingrowth, as demonstrated by the $^{206}Pb/^{204}Pb_{(i)}$ *vs* $^{87}Sr/^{86}Sr_{(i)}$ diagram reporting the initial isotopic values calculated at 30 Ma (Fig. 12d). The most extreme differences between bulk rock and coexisting clinopyroxenes are observed particularly in those picrites that clearly reflect crystal (ol+cpx) accumulation such as LAL70 and LAL73. For these samples, clinopyroxene crystals should not be considered real phenocrysts and could be interpreted as "antecrysts", i.e. phases that although grown in the same magmatic system did not crystallize directly from the host magma, thus recording marked isotopic disequilibrium. Similar disequilibrium evidences between cpx crystals and host rocks have been observed in other plume related magmas (Wei et al., 2015 and references therein).

Olivine phenocrysts from HT2 lavas (Table 5) have $^{3}He/^{4}He$ that range between 9.6 and 19.1 R_A with more than 50% of the analysed samples in the range 15.0-19.1 R_A. These values are significantly higher than those commonly observed in MORB (8 ± 1 R_A, Graham, 2002), in Ethiopian LT basalts (< 5 R_A) and in lavas from other African volcanic districts (Marty et al., 1996; Pik et al., 2006). Moreover, they are also higher than those recorded in mantle

xenoliths from the Afro-Arabian system (mostly in the range 6.5-8.0 R_A) which represent the local lithospheric mantle (Aulbach et al., 2011; Beccaluva et al., 2011b; Sgualdo et al., 2015). This He signature can be attributed to a deep, relatively undegassed mantle, although it is lower than the ratios measured in the Proto-Iceland plume picrites (up to 50 R_A, Stuart et al., 2003; Starkey et al., 2009). This may be the result of mixing with a low $^3He/^4He$ mantle end-member, also including recycled eclogite (< 0.1 R_A, Day et al., 2015).

Oxygen isotopic composition of olivine and clinopyroxene phenocrysts (Table 6) displays $\delta^{18}O$ values between 5.2 and 6.9 ‰ that are higher than those generally accepted for mineral phases in mantle derived magmas (Mattey et al., 1994). Similar values have been recorded in Yemeni CFB by Baker et al. (2000) and interpreted as the result of shallow level crustal contamination. However, in our opinion, they could be better attributed to the involvement of pyroxenite/eclogite lithologies in magma sources, as modelled in the previous section and suggested by $\delta^{18}O$ data on eclogite and metasomatized mantle xenoliths (Deines and Haggerty, 2000; Hao et al., 2015).

The possible involvement of Pan-African eclogite incorporated in the Afar plume has been tested using the available Sr and Nd isotopic data included in Berger et al. (2014) and those from lherzolite xenoliths from sub Ethiopian mantle (Beccaluva et al., 2011b). Mass balance calculation between these two end-members (lherzolite $^{87}Sr/^{86}Sr$ = 0.7029, $^{143}Nd/^{144}Nd$ = 0.5132; eclogite $^{87}Sr/^{86}Sr$ = 0.7056, $^{143}Nd/^{144}Nd$ = 0.5128) indicates that a mixture of ca. 11-13% eclogite and 89-87% lherzolite satisfactorily match the Sr-Nd isotopic composition of HT2 lavas. Unfortunately, Pb isotopes are not available for these eclogites but radiogenic Pb isotopic composition, compatible with that inferred for HT2 magma sources, have been reported for other eclogitized garnet-pyroxenites included in Pan-African terranes (Schmädicke et al., 2015). These mixture proportions are also compatible for the oxygen isotopes if we assume 5.2 as $\delta^{18}O$ value for lherzolite (Mattey et al., 1994) and 9.0 for pyroxenite/eclogite recycled component (Pearson et al., 1991). We may conclude that, based

on the available data, the source mixture resulting from isotopic mass-balance is in reasonable agreement with that inferred from trace element modelling discussed in the previous section (15% eclogite, 85% lherzolite).

7. Discussion and Conclusions

Detailed petrological and geochemical studies on the HT2 picrite-basalt lavas erupted at the core of the Ethiopian-Yemeni CFB plateau, and comparison with the associated HT1 and LT basalts, allow the thermo-compositional effects induced by the Oligocene Afar plume in the respective magma sources to be constrained.

Major element modelling and phase equilibria constraints on selected HT2 lavas indicate that picritic primary melts formed by partial melting of a garnet bearing mantle source in the pressure range 4-5 GPa, at potential temperature (T_p) of 1570°C. Fractional crystallization modelling (Fig. 6 and 8) shows that the observed differentiation trends from primary picrites to the most fractionated basalts can be accounted for by relatively low pressure polybaric fractionation, which likely occurred from the base of the continental crust (< 1 GPa), where upward advection of magma slowed down allowing more effective cooling. Accordingly, equilibrium olivine should appear on the liquidus at temperature of ca. 1510°C (Fo 91.3), as a result of nearly adiabatic uprising of primary magmas from the source region (T_p 1570°C, P_{min} 4 GPa, 0.6°C/km adiabatic gradient) up to the Moho (35-40 km). The most differentiated basaltic compositions were satisfactorily reproduced after removal of ca. 50% solid phases represented by olivine and clinopyroxene, the latter appearing on the cotectic at ca. 1260°C, *i.e.* at the picrite-basalt transition. However, it is noteworthy that the compositional variability of the HT2 lavas (and MI in olivine) appears to be related to widespread accumulation/disequilibrium crystallization and mutual magma mixing at crustal levels. This is also indicated by the wide $Kd_{Ol/Cpx\text{-}melt}$ range, the cross-cutting incompatible element cpx patterns, as well as the significant isotopic differences between Cpx and the host bulk rock

often recorded in HT2 lavas. This scenario conforms to a high magma production rate of basic melts rising along the same feeding system at the plume axial zone.

The thermal regime of the plateau outer zones was significantly cooler with respect to the inner part, as indicated by P-T genetic conditions of LT primary magmas (T_p 1430°C, <2 to 3 GPa), thus suggesting a thermal difference of 140°C between the axial and peripheral zones of the plume head. The spatial distribution of the Ethiopian-Yemeni CFB, and their P-T-X genetic conditions allow to reconstruct the Oligocene configuration of the Afar plume head as a melting region where plume-related thermo-chemical effects decreased outward (Fig. 14~~3~~). In particular, the anomalously high Ti, together with Fe and incompatible element enrichments, of the HT2 picrite-basalt suite imply the presence of peculiar components that enriched the relative mantle sources. A careful review of Fe-Ti reservoirs -such as pyroxenites/eclogites included in the upper mantle lithologies and/or relics of subducted oceanic lithosphere (*e.g.* ophiolites)- reveals that the best candidate to hybridize the HT2 mantle source is represented by eclogites derived from Transitional-MORB protoliths subducted during the Neo-Proterozoic, and currently outcropping in Pan-African terranes (Berger et al., 2014). Model calculations indicate that HT2 primary magmas could be generated by ca. 10% partial melting of a "piclogite" (*cf* Bianchini et al., 2010 and references therein) mantle source composed by 85% garnet lherzolite and 15% of the above mentioned eclogite. The inferred source characteristics do not conflict with the subchondritic $^{187}Os/^{188}Os$ ratio observed in HT2 Ethiopian picrites by Rogers et al. (2010), who limit to 15% and ≤ 1Ga in age, the possible contribution of Neo-Proterozoic subduction-related material in the source of the Ethiopian picrites. Accordingly, recent seismic tomography investigations seem to confirm the presence of a low velocity zone, at ca. 500 km beneath the Afar (Thompson et al., 2015), that in our opinion could represent piclogite domains stored at the mantle transition zone, partially remobilized and entrained by the Oligocene plume, and still persisting beneath the region.

The isotopic analyses extensively carried out on LT, HT1 and HT2 lavas reveal that while $^{143}Nd/^{144}Nd$ is rather homogeneous in the various magma types, Sr-Pb isotope ratios are positively correlated with TiO_2 reflecting the relative contribution of the pre-existing lithosphere and incoming sub-lithospheric plume components which increase from peripheral LT to the axial zone HT2 lavas (Fig. 13). Accordingly, the Afar plume fingerprint is particularly recorded by HT2 picrite-basalt magmas that are characterized by a limited isotopic variability, and cluster between the notional DM and EM2 mantle end-members. Coherently, this isotopic signature is recorded in mantle xenoliths from the plateau area (Beccaluva et al., 2011b; Bianchini et al., 2014) and still persists in the recent Afar volcanism (Rooney et al., 2012). By contrast, Neogene volcanics and associated mantle xenoliths from Afro-Arabian domains located outside from the Ethiopian-Yemeni plateau display a much wider isotopic spectrum mainly varying between the DM, HIMU and EM1 end-members (Furman et al., 2006; Rogers, 2000; Beccaluva et al., 2011b; Bianchini et al., 2014; Sgualdo et al., 2015).

The new He isotopic data are in accordance with literature data that recorded $^{3}He/^{4}He$ up to 20 R_A in the same lava type (Marty et al., 1996; Pik et al., 2006). We tentatively explain this as a mixing of mantle plume, "normal" mantle domains and recycled eclogite. The involvement of the latter is corroborated by the recorded O isotopic compositions that display values that are higher than those generally observed in magmas derived from purely peridotitic mantle.

Therefore, the Ethiopian-Yemeni province may represent a typical well constrained example of a LIP generated by a hot mantle plume. It entrained eclogitic and undegassed components, ultimately leading to a plume head with decreasing thermo-chemical effects over a radial extension of ca. 400 km, from which zonally arranged CFB were generated.

The worldwide comparison of high-MgO lavas from various CFB Phanerozoic provinces (Fig. 8 and 10a) indicates that these magmas shares high mantle potential temperatures (T_p

1550-1700°C) supporting the existence of plume related thermal anomalies as triggering events for the rapid emplacement of large volume of basic magmas, that often preceded continental break-up and oceanic opening. However, thermal anomalies are not necessarily accompanied by strong geochemical signature (e.g. Ti and incompatible element enrichments), thus suggesting that mantle plumes exert variable, sometimes weak, chemical effect on the lithospheric CFB magma sources. This could explain the difficulty to recognize a precise plume fingerprint in some CFB occurrences as is the case of ferropicrite dykes from Vestfjella, that are at least in part isotopically indistinguishable from MORB of the SW Indian Ridge (Heinonen et al., 2010). Similarly, low-Ti and high-Ti CFB of the Parana province (ca. 130 Ma) although overlapping the "Tristan plume" isotopic signature (Thompson et al., 2001), also record significant compositional and isotopic (Sr-Nd) similarities with Late Archean-Proterozoic and Early Jurassic (CAMP, ca. 200 Ma) tholeiites from the South American platform (Iacumin et al., 2003). We may conclude that, although the mantle plume hypothesis represents a suitable explanation for generating many LIP characterized by high-T and high eruption rate of CFB, the reliable assignment of specific geochemical components to mantle plume effects should be based on extensive and detailed investigations of the spatial-temporal distribution and thermo-compositional features of the entire magmatic province.

Acknowledgments

Thanks are due to the colleagues of the University of Addis Ababa G. Yirgu, D. Ayalew, T. Ayenew, B. Abebe and A. Asrat for support and fruitful discussions, and to M. Al-Kadasi of the Sana'a University for logistic support during the field trip in Yemen. Special thanks go to the staff of the Dipartimento di Scienze della Terra, Università di Ferrara; in particular, R. Tassinari is gratefully acknowledged for its support with the XRF and ICP-MS analyses. Many thanks go to R. Carampin (CNR-IGG, Padua) and A. Zanetti (CNR-IGG, Pavia) that

supervised the EMPA and LA-ICP-MS analyses. As concern isotope analyses, thanks are given to A. Kelly, L. Di Nicola and V. Gallagher (SUERC), S. Tonarini and L. Dallai (CNR-IGG, Pisa). The authors also thank B. Bonin and other two anonymous reviewers, as well as the editor I. Safonova for the constructive comments that greatly improved the manuscript.

References

Asprey, L.B., 1976. The preparation of very pure F2 gas. Journal of Fluorine Chemistry 7, 359–361.

Aulbach, S., Rudnick, R.L., McDonough, W.F., 2011. Evolution of the lithospheric mantle beneath the East African Rift in Tanzania and its potential signatures in rift magmas. Geological Society of America (GSA) Special Paper 478, 105–125.

Baker, J., Snee, L. & Menzies, M., 1996. A brief Oligocene period of flood volcanism in Yemen: implications for the duration and rate of continental flood volcanism at the Afro-Arabian triple junction. Earth and Planetary Science Letters 138, 39-55.

Baker, J. A., Macpherson, C. G., Menzies, M. A., Thirlwall, M. F., Al-Kadasi, M., Mattey, D. P., 2000. Resolving crustal and mantle contributions to continental flood volcanism, Yemen; constraints from mineral oxygen isotope data. Journal of Petrology 41, 1805-1820.

Bastow, I.D., Nyblade A., Stuart G.W., Rooney T.O., Benoit M.H., 2008. Upper mantle seismic structure beneath the Ethiopian hot spot: Rifting at the edge of the African low-velocity anomaly. Geochemistry, Geophysics, Geosystems 9, Q12022, doi:10.1029/2008GC002107.

Bastow, I.D., Keir, D., Daly, E., 2011. The Ethiopia Afar Geoscientific Lithospheric Experiment (EAGLE): probing the transition from continental rifting to incipient seafloor spreading. Geological Society of America (GSA) Special Paper 478, 51–76.

Beccaluva, L., Bianchini, G., Natali, C., Siena, F., 2009. Continental flood basalts and mantle plumes: a case study of the northern Ethiopian plateau. Journal of Petrology 50, 1377–1403.

Beccaluva, L., Bianchini, G., Wilson, M., 2011a. Volcanism and Evolution of the African Lithosphere. Geological Society of America, Special Paper 478, 331 pp.

Beccaluva, L., Bianchini, G., Ellam, R.M., Natali, C., Santato, A., Siena, F., Stuart, F.M., 2011b. Peridotite xenoliths from Ethiopia: inferences about mantle processes from plume to rift settings. Geological Society of America (GSA) Special Paper 478, 77–104.

Bellahsen, N., Faccenna, C., Funiciello, F., Daniel, J.M., Jolivet, L., 2003. Why did Arabia separate from Africa? Insights from 3-D laboratory experiments. Earth and Planetary Science Letters 216, 365-381.

Berger, J., Ouzegane, K., Bendaoud, A., Liégeois, J-P., Kiénast, J-R., Bruguier, O., Caby, R., 2014. Continental subduction recorded by Neoproterozoic eclogite and garnet amphibolites from Western Hoggar (Tassendjanet terrane, Tuareg Shield, Algeria). Precambrian Research 247, 139-158.

Bianchini, G., Beccaluva, L., Bonadiman, C., Nowell, G.M., Pearson, D.G., Siena, F., Wilson, M., 2010. Mantle metasomatism by melts of HIMU piclogite components: new insights from Fe-lherzolite xenoliths (Calatrava Volcanic District, Central Spain). London Geological Society, Special Publication 337, 107-124.

Bianchini, G., Bryce, J., Blichert-Toft, J., Beccaluva, L., Natali, C., 2014. Mantle dynamics and secular variations beneath the East African Rift: insights from peridotite xenoliths (Mega, Ethiopia). Chemical Geology 386, 49–58.

Bosworth, W., Huchon, P., McClay, K., 2005. The Red Sea and Gulf of Aden Basins. Journal of African Earth Sciences 43, 334–378.

Buslov, M.M., Safonova, I.Yu., Fedoseev, G.S., Reichow, M.K., Davies, K. & Babin, G.A. 2010. Permo-Triassic plume magmatism of the Kuznetsk Basin, Central Asia: geology, geochronology, and geochemistry. Russian Geology and Geophysics 51, 1021–1035.

Campbell, I.H., Davies G.F., 2006. Do mantle plumes exist? Episodes 29, 162–168.

Carlson, R.W., Czamanske, G., Fedorenko, V., Ilupin, I., 2006. A comparison of Siberian Meimechites and kimberlites: implications for the source of high-Mg alkalic magmas and flood basalts. Geochemistry Geophysics Geosystems 7, Q11014. doi:10.1029/2006GC001342.

Chang, S.-J., Van der Lee, S., 2011. Mantle plumes and associated flow beneath Arabia and East Africa. Earth and Planetary Science Letters 302, 448–454.

Coltice, N., Bertrand, H., Rey, P., Jourdan, F., Phillips, B.R., Ricard Y., 2009. Global warming of the mantle beneath continents back to the Archaean. Gondwana Research 15, 254–266.

Conticelli, S., Sintoni, M.F., Abebe, T., Mazzarini, F., Manetti, P., 1999. Petrology and geochemistry of ultramafic xenoliths and host lavas from the Ethiopian Volcanic Province: An insight into the upper mantle under eastern Africa. Acta Vulcanologica 11, 143-159.

Coogan, L.A., Saunders, A.D., Wilson, R.N. 2014. Aluminum-in-olivine thermometry of primitive basalts: evidence of an anomalously hot mantle source for large igneous provinces. Chemical Geology 368,1–10.

Courtillot, V., Davaille, A., Besse J., Stock, J., 2003. Three distinct types of hotspots in the Earth's mantle. Earth and Planetary Science Letters 205, 295-308

Danyushevsky, L.V., Plechov, V., 2011. Petrolog3: Integrated software for modeling crystallization processes. Geochemistry, Geophysics, Geosystems 12, DOI: 10.1029/2011GC003516.

Danyushevsky, L.V., McNeill, A.W., Sobolev, A.V., 2002. Experimental and petrological studies of melt inclusions in phenocrysts from mantle-derived magmas: an overview of techniques, advantages and complications. Chemical Geology 183, 5–24.

Davaille, A., Stutzmann, E., Silveira, G., Besse, J. & Courtillot, V., 2005. Convective patterns under the Indo-Atlantic ‘box’. Earth and Planetary Science Letters 239, 233-252.

Day, J.M.D., Barry, P.H., Hilton, D.R., Pearson, D.G., Burgess, R., Taylor, L.A., 2015. The helium flux from the continents and ubiquity of low-3He/4He recycled crust and lithosphere. Geochimica et Cosmochimica Acta 153, 116-133.

Del Moro, S., Di Roberto, A., Meletlidis, S., Pompilio, M., Bertagnini, A., Agostini, S., Ridolfi, F., Renzulli, A., 2015. Xenopumice erupted on 15 October 2011 offshore of El Hierro (Canary Islands): a subvolcanic snapshot of magmatic, hydrothermal and pyrometamorphic processes. Bulletin of Volcanology 77, doi:10.1007/s00445-015-0940-0.

Desta, M.T., Ayalew, D., Ishiwatari, A., Arai, S., Tamura, A., 2014. Ferropicrite from the Lalibela area in the Ethiopian large igneous province. Journal of Mineralogical and Petrological Science 109, 191-207.

Deines, P., Haggerty, S., 2000. Small-scale oxygen isotope variations and petrochemistry of ultradeep (>300 km) and transition zone xenoliths. Geochimica et Cosmochimica Acta 64, 117–131.

Ebinger, C.J., Sleep, N.H., 1998. Cenozoic magmatism throughout East Africa resulting from impact of a single plume. Nature 395, 788-791.

Elkins-Tanton, L.T., Van Orman, J.A., Hager, B.H., Grove, T.L. 2002. Re-examination of the Lunar Magma Ocean cumulate overturn hypothesis: melting or mixing is required. Earth and Planetary Science Letters 196, 239–249.

Elkins-Tanton, L.T., Burgess, S., Yin, Q.-Z. 2011. The lunar magma ocean: Reconciling the solidification process with lunar petrology and geochronology. Earth and Planetary Science Letters 304, 326-336.

Ellam, R.M., 2006. New constraints on the petrogenesis of the Nuanetsi picrite basalts from Pb and Hf isotope data. Earth and Planetary Science Letters 245, 153–161.

Ellam, R.M., Cox, K.G., 1991. An interpretation of Karoo picrite basalts in terms of interaction between asthenospheric magmas and the mantle lithosphere. Earth and Planetary Science Letters 105, 330-342.

Ellam, R.M., Carlson, R.W., Shirey, S.B., 1992. Evidence from Re-Os isotopes for plume lithosphere mixing in Karoo flood basalt genesis. Nature 359, 718-721.

Ernst, R.E., Buchan, K.L., 2001a. Mantle Plumes: Their Identification Through Time. Geological Society of America, Special Paper 352, 593 pp.

Ernst, R.E., Buchan, K.L., 2001b. Large mafic magmatic events through time and links to mantle plume heads. Geological Society of America (GSA) Special Paper 352, 483–576.

Farmer, G.L., 2003. Continental basaltic rocks. In: Rudnick, L.R. (ed.) Treatise on Geochemistry,Volume 3,The Crust. Oxford: Elsevier-Pergamon, pp. 85-121.

Foulger, G.R., Jurdy, D.M., 2007. Plates, Plumes and Planetary Processes. Geological Society of America, Special Paper 430, 997 pp.

Foulger, G.R., Natland, J.H., Presnall, D.C., Anderson, D.L., 2005. Plates, Plumes and Paradigms. Geological Society of America, Special Paper 388, 881 pp.

Furman, T., Bryce, J., Rooney, T., Hanan, B., Yirgu, G., Ayalew, D., 2006. Heads and tails: 30 My of the Afar plume. In: Yirgu, G., Ebinger, C. J. & Maguire, P. K. H. (eds) Structure and Evolution of the East African Rift System in the Afar Volcanic Province. Geological Society, London, Special Publications 259, 97-121.

Gani, N.D., Gani, M.R., Abdelsalam, M.G., 2007. Blue Nile incision on the Ethiopian Plateau: Pulsed plateau growth, Pliocene uplift, and hominin evolution. GSA Today 17, 4-11.

Gibson, S.A., Thompson, R.N., Dickin, A.P., 2000. Ferropicrites: Geochemical evidence for Fe-rich streaks in upwelling mantle plumes: Earth and Planetary Science Letters 174, 355–374.

Graham, D.W., 2002. Noble gas isotope geochemistry of mid-ocean ridge and ocean island basalts; characterization of mantle source reservoirs. In: Porcelli, D., Wieler, R., Ballentine, C.J. (eds.), Noble Gases in Geochemistry and Cosmochemistry. Mineral. Soc. Amer. Reviews in Mineralogy and Geochemistry, Washington, D.C., pp. 247–318.

Green, D.H., Falloon, T.J., 2005. Primary magmas at mid-ocean ridges, 'hotspots', and other intraplate setting: Constraints on mantle potential temperature. In: Foulger, G. R., Natland, J.H., Presnall, D.C., Anderson, D.L. (eds) Plates, Plumes, and Paradigms. Geological Society of America, Special Papers 388, 217-247.

Gudfinnson, G.H., Presnall, D.C., 2005. Continuous gradations among primary carbonatitic, kimberlitic, melilitic, basaltic, picritic and komatiitic melts in equilibrium with garnet lherzolite at 3-8 GPa. Journal of Petrology 46, 1646-1659.

Hao, Y-T., Xia, Q-K., Dallai, L., Coltorti, M., 2015. Recycled oceanic crust-derived fluids in the lithospheric mantle of eastern China: Constraints from oxygen isotope compositions of peridotite xenoliths. Lithos 228-229, 55-61.

Hardarson, B.S., Fitton, J.G., Ellam, R.M., Pringle, M.S., 1997. Rift relocation—A geochemical and geochronological investigation of a palaeo-rift in northwest Iceland: Earth and Planetary Science Letters 153, 181–196.

Heinonen, J.S., Luttinen, A.V., 2008. Jurassic dikes of Vestfjella, western Dronning Maud Land, Antarctica: Geochemical tracing of ferropicrite sources. Lithos 105, 347-364.

Heinonen, J.S., Carlson, R.W., Luttinen, A.V., 2010. Isotopic (Sr, Nd, Pb, and Os) composition of highly magnesian dikes of Vestfjella, western Dronning Maud Land, Antarctica: A key to the origins of the Jurassic Karoo large igneous province? Chemical Geology 277, 227-244.

Heinonen, J.S., Luttinen, A.V., Riley, T.R., Michallik, R.M., 2013. Mixed pyroxenite–peridotite sources for mafic and ultramafic dikes from the Antarctic segment of the Karoo continental flood basalt province. Lithos 177, 366-380.

Heinonen, J.S., Carlson, R.W., Riley, T.R., Luttinen, A.V., Horan, M.F. (2014). Subduction-modified oceanic crust mixed with a depleted mantle reservoir in the sources of the Karoo continental flood basalt province. Earth and Planetary Science Letters 394, 229-241.

Heinonen, J.S., Jennings, E.S., Riley, T.R. 2015. Crystallisation temperatures of the most Mg-rich magmas of the Karoo LIP on the basis of Al-in-olivine thermometry. Chemical Geology 411, 26-35.

Herzberg, C., Asimow, P.D., 2015. PRIMELT3 MEGA.XLSM software for primary magma calculation: Peridotite primary magma MgO contents from the liquidus to the solidus. Geochemistry, Geophysics, Geosystem 8, DOI: 10.1002/2014GC005631.

Herzberg, C., O'Hara, M.J., 2002. Plume associated magmas of Phanerozoic age. Journal of Petrology 43, 1857-1883.

Herzberg, C., Zhang, J., 1996. Melting experiments on anhydrous peridotite KLB-1: Compositions of magmas in the upper mantle and transition zone. Journal of Geophysical Research 101, 8271-8295.

Herzberg, C., Asimow, P.D., Arndt, N., Niu, Y., Lesher, C.M., Fitton, J.G., Cheadle, M.J., Saunders, A.D., 2007. Temperatures in ambient mantle and plumes: Constraints from basalts, picrites and komatiites: Geochemistry Geophysics Geosystems 8, doi:10.1029GC001390.

Hofmann, A.W., 1997. Mantle geochemistry: the message from oceanic volcanism. Nature 385, 219-229.

Hofmann, C., Courtillot, V., Feraud, G., Rochette, P., Yirgu, G., Ketefo, E., Pik, R., 1997. Timing of the Ethiopian flood basalt event and implications for plume birth and global change. Nature 389, 838-841.

Iacumin, M., De Min, A., Piccirillo, E.M., Bellieni, G., 2003. Source mantle heterogeneity and its role in the genesis of Late Archean-Proterozoic (2.7-1.0 Ga) and Mesozoic (200 and 130 Ma) tholeiitic magmatism in the south American Platform. Earth-Science Reviews 62, 365-397.

Jackson, M.G., Carlson, R., 2011. An ancient recipe for flood basalt genesis. Nature 476, 316-319.

Jeffries, T.E., Perkins, W.T., Pearce, N.J.G., 1995. Measurements of trace elements in basalts and their phenocrysts by laser probe microanalysis inductively coupled plasma mass spectrometry (LPMA-ICP-MS). Chemical Geology 121, 131-144.

Jennings, E.S., Gibson, S.A., Maclennan, J. 2014. The origin of Ferropicrite: High pressure melting of mantle pyroxenite beneath continental lithosphere. Goldschmidt Conference, Abstract Volume, p. 1130.

Jennings, E.S., Gibson, S.A., Maclennan, J., Heinonen, J.S., Luttinen, A.V., Riley, T.R. 2014. Picrites and Ferropicrites: Mantle heterogeneity in a continental flood basalt setting. Volcanic and Magmatic Studies Group (VMSG) – Annual Meeting, Edinburgh, B002.

Kamenetsky, V.S., Chung, S.-L., Kamenetsky, M.B., Kuzmin, D.V., 2012. Picrites from the Emeishan Large Igneous Province, SWChina: a compositional continuum in primitive magmas and respective mantle sources. Journal of Petrology 53, 2095–2113.

Kieffer, B., Arndt, N., Lapierre, H., Bastien, F., Bosch, D., Pecher, A., Yirgu, G., Ayalew, D., Weis, D., Jerram, D. A., Keller, F., Meugniot, C., 2004. Flood and shield basalts from Ethiopia: magmas from the African Superswell. Journal of Petrology 45, 793-834.

Le Roex A.P., 1987. Source region of mid-ocean ridge basalts: evidence for enrichment processes. In: Menzies M.A., Hawkesworth C.J. (eds.), Mantle metasomatism. Academic Press, London, p. 389-419.

Marty, B., Pik, R., Yirgu, G.,. 1996. Helium isotopic variations in Ethiopian plume lavas: nature of magmatic sources and limit on lower mantle contribution. Earth and Planetary Science Letters 144, 223–237.

Mattey, D.P., Lowry D., Macpherson C., 1994. Oxygen isotope composition of mantle peridotite. Earth and Planetary Science Letters 128, 231-241.

Mège, D., Korme, T., 2004. Dyke swarm emplacement in the Ethiopian large igneous province: not only a matter of stress. Journal of Volcanology and Geothermal Research, 132, 283–310.

Melluso, L., Beccaluva, L., Brotzu, P., Gregnanin, A., Gupta, A.K., Morbidelli, L., Traversa, G., 1995. Constraints on the mantle sources of the Deccan Traps from the petrology and geochemistry of the basalts of Gujarat State (Western India). Journal of Petrology 36, 1393-1432.

Moucha, R., Forte, A.M., 2011. Changes in African topography driven by mantle convection, Nature Geoscience 4, 707-712.

Natali, C., Beccaluva, L., Bianchini, G., Siena, F., 2011. Rhyolites associated to Ethiopian CFB: clues for initial rifting at the Afar plume axis. Earth and Planetary Science Letters 312, 59–68.

Natali, C., Beccaluva, L., Bianchini, G., Siena, F., 2013. The Axum–Adwa basalt–trachyte complex: a late magmatic activity at the periphery of the Afar plume. Contribution to Mineralogy and Petrology 166, 351-370.

Pik, R., Daniel, C., Coulon, C., Yirgu, G., Hofmann, C., Ayalew, D., 1998. The northwestern Ethiopian flood basalts: classification and spatial distribution of magma types. Journal of Volcanology and Geothermal Research 81, 91–111.

Pik, R., Marty, B., Hilton, D.R., 2006. How many plumes in Africa? The geochemical point of view. Chemical Geology 226, 100–114.

Pik, R., Deniel, C., Coulon, C.,Yirgu, G., Marty, B., 1999. Isotopic and trace element signatures of Ethiopian flood basalts: evidence for plume-lithosphere interactions. Geochimica et Cosmochimica Acta 63, 2263-2279.

Reichow, M.K., Pringle, M.S., Al'Mukhamedov, A.I., Allen, M.B., Andreichev, V.L., Buslov, M.M., Davies, C.E., Fedoseev, G.S., Fitton, J.G., Inger, S., Medvedev, A.Ya., Mitchell, C., Puchkov, V.N., Safonova, I.Yu., Scott, R.A., Sauders, A.D. 2009. The timing and extent of the eruption of the Siberian traps large igneous province. Implication for the end-Permian environmental crisis. Earth and Planetary Science Letters 277, 9–20.

Révillon, S., Arndt, N. T., Hallot, E., Kerr, A. C., Tarney, J., 1999. Petrogenesis of picrites from the Caribbean plateau and the North Atlantic magmatic province. Lithos 49, 1–21.

Révillon, S., Arndt, N.T., Chauvel, C. & Hallot, E., 2000. Geochemical Study of Ultramafic Volcanic and Plutonic Rocks from Gorgona Island, Colombia: the Plumbing System of an Oceanic Plateau. Journal of Petrology 41, 1127-1153.

Rogers, N., 2006. Basaltic magmatism and the geodynamics of the East African rift system. In: Yirgu, G., Ebinger, C.J., Maguire, P.K.H. (eds) The Afar Volcanic Province within the East African Rift System. Geological Society, London, Special Publications 259, 77-93.

Rogers, N.W., Davies, M.K., Parkinson, I.J., Yirgu, G., 2010. Osmium isotopes and Fe/Mn ratios in Ti-rich picritic basalts from the Ethiopian flood basalt province: no evidence for core contribution to the Afar plume. Earth and Planetary Science Letters 296, 413–422.

Rooney, T.O., Hanan, B.B., Graham, D.W., Furman, T., Blichert-Toft, J., Schilling, J.-G., 2012. Upper mantle pollution during Afar plume—Continental rift interaction, Journal of Petrology 53, 365–389.

Rosenthal, A., Yaxley, G.M., Green, D.H., Hermann, J., Kovács, I., Spandler, C. 2014. Continuous eclogite melting and variable refertilisation in upwelling heterogeneous mantle. Scientific Reports 4, 6099.

Saccani, E., Allahyari, K., Beccaluva, L., Bianchini G., 2013. Geochemistry and petrology of the Kermanshah ophiolites (Iran): Implication for the interaction between passive rifting, oceanic accretion, and plume-components in the Southern Neo-Tethys Ocean. Gondwana Research 24, 392–411.

Safonova, I.Yu., Santosh, M. 2014. Accretion complexes in the Asia-Pacific region: Tracing archives of ocean plate stratigraphy and tracking mantle plumes. Gondwana Research 25, 126-158.

Şengor, A.M.C., 2001. Elevation as indicator of mantle plume activity. In: Ernst, R., Buchan, K. (eds) Mantle Plumes: their Identification through Time. Geological Society of America, Special Paper 352, 183-225.

Sheth, H.C. Zellmer, G.F., Demonterova, E.I., Ivanov, A.V., Kumar, R., Kumar Patel, R., 2014. The Deccan tholeiite lavas and dykes of Ghatkopar-Powai area, Mumbai, Panvel flexure zone: Geochemistry, stratigraphic status, and tectonic significance. Journal of Asian Earth Sciences 84, 69-82.

Sgualdo, P., Aviado, K., Beccaluva, L., Bianchini, G., Blichert-Toft, J., Bryce, J.G., Graham, D.W., Natali, C., Siena, F., 2015. Lithospheric mantle evolution in the Afro-Arabian domain: Insights from Bir Ali mantle xenoliths (Yemen). Tectonophysics 650, 3-17.

Sharp, Z.D., 1995. Oxygen isotope geochemistry of the Al_2SiO_5 polymorphs. American Journal of Science 295, 1058–1076.

Schmädicke, E., Will, T.M., Mezger K., 2015. Garnet-pyroxenite for the Shackleton Range, Antarctica: Intrusion of plume-derived picritic melts in the continental lithosphere during Rodinia breakup? Lithos 238, 185-206.

Sobolev, A.V., Hofmann, A.W., Kuzmin, D.V., Yaxley, G.M., Arndt, N.T., Chung, S.-L., Danyushevsky, L.V., Elliott, T., Frey, F.A, Garcia, M.O., Gurenko, A.A., Kamenetsky, V.S., Kerr, A.C., Krivolutskaya, N.A., Matvienkov, V.V., Nikogosian, I.K., Rocholl, A., Sigurdsson, I.A., Sushchevskaya, N.M., Teklay, M., 2007. The amount of recycled crust in sources of mantle-derived melts. Science 316, 412-417.

Sobolev, A.V., Sobolev, S.V., Kuzmin, D.V., Malitch, K.N., Petrunin, A.G., 2009. Siberian meimechites: Origin and relation to flood basalts and kimberlites, Russian Geology and Geophysics 50, 999–1033.

Solomatov, V.S. 2016. The terrestrial magma ocean hypothesis. Gondwana Research (in press). http://dx.doi.org/10.1016/j.gr.2015.07.018

Starkey, N.A., Stuart, F.M., Ellam, R.M., Fitton, J.G., Basu, S., Larsen, L.M., 2009. Helium isotopes in early Iceland plume picrites: Constraints on the composition of high-3He/4He mantle. Earth and Planetary Science Letters 277, 91-100.

Stuart, F.M., Ellam, R.M., Harrop, P.J., Fitton, J.G., Bell, B.R., 2000. Constraints on mantle plumes from the helium isotopic composition of basalts from the British Tertiary igneous province. Earth and Planetary Science Letters 177, 273–285.

Stuart, F.M., Lass-Evans, S., Fitton, J.G., Ellam, R.M., 2003. High 3He/4He ratios in picritic basalts from Baffin Island and the role of a mixed reservoir in mantle plumes. Nature 424, 57–59.

Sun, S.S., McDonough, W.F., 1989. Chemical and isotopic systematics of oceanic basalts: implications for mantle composition and processes. In: Saunders, A.D. Norry, M.J. (eds) Magmatism in the Ocean Basins. Geological Society, London, Special Publications 42, 313-347.

Stern, R.J., Johnson P., 2010. Continental lithosphere of the Arabian Plate: A geologic, petrologic, and geophysical synthesis, Earth Science Reviews 101, 29–67.

Stracke, A., Hofmann, A., Hart, S., 2005. FOZO, HIMU, and the rest of the mantle zoo. Geochemistry, Geophysics, Geosystems 6, DOI: 10.1029/2004GC000824.

Tanaka, T., Togashi, S., Kamioka, H., et al., 2000. JNdi-1; a neodymium isotopic reference in consistency with La Jolla neodymium. Chemical Geology 168, 279–281.

Teklay, M., Asmerom, Y., Toulkeridis, T., 2005. Geochemical and Sr-Nd isotope ratios in Cenozoic basalts from Eritrea: evidence for temporal evolution from low-Ti tholeiitic to high-Ti alkaline basalts in Afro-Arabian Continental Flood Basalt Province. Periodico di Mineralogia 74, 167-182.

Thompson, D.A., Hammond, J.O.S., Kendall, J.M., Stuart, G.W., Helffrich, G.R., Keir, D., Ayele, A., Goitom, B., 2015. Hydrous upwelling across the mantle transition zone beneath the Afar Triple Junction. Geochemistry, Geophysics, Geosystems 16, 834-846.

Thompson, R.N., Gibson, S.A., Dickin, A.P., and Smith, P.M., 2001. Early Cretaceous basalt and picrite dikes of the southern Etendeka region, NW Namibia: Windows into the role of the Tristan mantle plume in Paraná–Etendeka magmatism: Journal of Petrology 42, 2049–2081.

Thompson, R.N., Gibson, S.A., 2000. Transient high temperatures in mantle plume heads inferred from magnesian olivines in Phanerozoic picrites. Nature 407, 502–506.

Todt, W, Cliff, R.A., Hanser, A., Hofmann, A.W., 1993. Re-calibration of NBS lead standards using a ^{202}Pb-^{205}Pb double spike. Geophysical Monographs 95, 429-437

Tuff, J.,Takahashi, E., Gibson, S.A., 2005. Experimental constraints on the role of garnet pyroxenite in the in the genesis of High-Fe mantle plume derived melts. Journal of Petrology 46, 2223-2258.

Ukstins, I., Renne, P., Wolfenden, E., Baker, J., Ayalew, D., Menzies, M.A., 2002. Matching conjugate volcanic rifted margins: 40Ar/39Ar chronostratigraphy of pre- and syn-rift

bimodal flood volcanism in Ethiopia and Yemen. Earth and Planetary Science Letters 198, 289-306.

Walter (1998) Melting of garnet peridotite and the origin of komatiite and depleted lithosphere. Journal of Petrology 39, 29-60.

Weaver, B.L., 1991. The origin of ocean island end-member compositions: trace element and isotopic constraints. Earth and Planetary Science Letters 104, 381-397.

Wei, X., Xu, Y-G, Luo, Z-Y, Zhao, J-X, Feng, Y-X., 2015. Composition of the Tarim mantle plume: constraints from clinopyroxene antecrysts in the early Permian Xiaohaizi dykes, NW China. Lithos 230, 69-81.

Yirgu, G., Ebinger, C.J., Maguire, P.K.H. (eds) (2006). The Afar Volcanic Province within the East African Rift System. Geological Society, London, Special Publications 259, 327 pp.

Zhang, Y., Liu, J., Guo, Z., 2010. Permian basaltic rocks in the Tarim basin, NW China: Implications for plume-lithosphere interaction. Gondwana Research 18, 596-610.

Table captions

Table 1 – Bulk rock major and trace element composition of HT2 basalts and picirites from the Ethiopian-Yemeni CFB.

Footnote: $Fe_2O_3/FeO= 0.15$; mg# = (MgO)/(MgO+FeO) mol%. * = analyses from Beccaluva et al. (2009) and Natali et al. (2011). ** = corrected for typing error in Beccaluva et al. (2009).

Table 2 – Major (EMPA) and trace element (LA-ICP-MS) averaged analyses of melt inclusions (MI) in olivine and interstitial glass (Gl) from Ethiopian HT2 basalts and picrites.

Table 3 – LA-ICP-MS trace element analyses of clinopyroxene in HT2 picrites and basalts from Ethiopian-Yemeni CFB.

Table 4 – Sr-Nd-Pb isotopic composition of LT, HT1 and HT2 lavas and separated clinopyroxenes from the Ethiopian-Yemeni CFB.

Footnote: Sr, Nd and Pb initial isotope ratios, calculated at 30 Ma, are also reported.

Table 5 – $^{3}He/^{4}He$ composition of olivine from Ethiopian HT2 lavas.

Footnote: Measured ratios (R) are normalized to the atmospheric ratio (Ra; 1.384×10^{-6}). Uncertainties are expressed as 1σ.

Table 6 – $\delta^{18}O$ of olivine and clinopyroxene separated from Ethiopian HT2 lavas.

Footnote: Uncertainties are expressed as 1σ.

Supplementary Table 1 – Representative analyses of constituent minerals from HT2 picrite-basalt lavas. a) olivine, b) clinopyroxene, c) feldspars, d) Fe-Ti-Cr oxides, e) phlogopite and amphibole.

Figure captions

Figure 1 – Sketch map of the Oligocene Ethiopian-Yemeni CFBs (modified after Beccaluva et al., (2009); other data from Baker et al. (1996), Pik et al. (1998), Kieffer et al. (2004), Teklay et al. (2005) and Natali et al. (2011). LT = Low-Ti tholeiites, HT1 = High-Ti tholeiites, HT2 = very High-Ti transitional basalts and picrites. Sampling locations are

indicated by circles (LT basalts), triangles (HT1 basalts), diamonds (HT2 basalts) and squares (HT2 picrites). Miocene volcanoes overlapping CFBs are also reported. A paleogeographic restoration at the Oligocene of the original Ethiopian-Yemeni plateau displaying a contiguous zonal arrangement of LT, HT1 and HT2 lavas is reported in the inset.

Figure 2 – Total Alkali-Silica (TAS) classification diagram for the Ethiopian-Yemeni CFBs. The dashed line subdivides the alkaline and subalkaline series. LT = Low-Ti tholeiitic basalts, HT1 = High-Ti tholeiitic basalts, HT2 = very High-Ti transitional basalts (diamonds) and picrites (squares), MI = Melt Inclusions in olivine from HT2 picrite and basalt, Gl = interstitial Glasses from picrite LAL73.

Figure 3 – FeO_t, TiO_2, Nb and Ce vs MgO variation diagrams for Ethiopian-Yemeni CFB (large symbols from Author data base; small symbols from Baker et al., 1996; Pik et al., 1998; Teklay et al., 2005). Empirical boundaries between LT, HT1 and HT2 are drawn in order to minimize the misclassified samples (generally less than 5%). Clear compositional variations between magma types can be interpreted in terms of intergroup source enrichments and fractionation trends. Symbols and other abbreviations as in Fig. 1 and 2.

Figure 4 – Ch-Normalized REE patterns (a) and PM-Normalized incompatible elements distribution (b) of HT2 lavas from Ethiopian-Yemeni CFB. The PM-Normalized distribution of melt inclusions (MI) in olivine and interstitial glass (Gl) is reported in (c) and compared with the compositional field of HT2 picrites (shaded area). Normalizing factors from Sun & McDonough (1989). See text for further details.

Figure 5 – Ch-Normalized REE patters of clinopyroxenes from HT2 picrites (a) and basalts (b) from the Ethiopian-Yemeni CFB. The same symbol is referred to different clinopyroxene

analyses from the same rock sample. Note that clinopyroxenes from the Yemeni HT2 basalt (x), show the highest incompatible element patterns consistent with their comparatively more alkaline character. Normalizing factors from Sun & McDonough (1989).

Figure 6 – MgO *vs* FeO diagram for the Ethiopia-Yemeni CFB. HT2, HT1 and LT primary magmas are modelled according to Herzerberg and Asimow (2015). Several liquid lines of descent (Petrolog3, Danyuschevsky and Plechov, 2011) satisfactorily match the observed compositional variations; the HT2, HT1 and LT suites result from Ol+Cpx, Ol+Cpx+Pl and Ol+Pl+Cpx fractionation trends, respectively (inset). For comparison, calculated primary magmas and related compositional fields (shaded areas) of lavas from East Pacific Rise (EPR), Iceland, Hawaii and Gorgona, together with equilibrium olivine arrays, are also shown (modified after Herzberg et al., 2007 and references therein).

Figure 7 – Fo_{Ol} *vs* $Mg\#_{bulk\ rock}$ for HT2 Ethiopian-Yemeni basalts and picrites. Tie lines join multiple olivine composition recorded in the same rock sample. Note that most of the olivine analyses in picrites show lower Fo contents than expected from equilibrium $Kd_{Mg\text{-}Fe}$ (0.28-0.32), as effect of olivine accumulation.

Figure 8 – Temperature (°C) *vs* MgO (wt%) petrogenetic grid for HT2 and LT suites based on modelling described in Fig. 6. The hypothetical thermo-compositional evolution from HT2 primary melts (dark grey field) to the most differentiated basalt is depicted by trend 1: modelling matches the composition of the most forsteritic olivine observed in equilibrium with the host picrite for pressure < 1GPa. In principle this imply that primary magmas (*ca.* 1570°C) raised nearly-adiabatically up to the base of the crust (35-40 km), where the olivine liquidus was reached at temperature of *ca.* 1510°C. Fractional crystallization process was mainly controlled by olivine down to 1250°C where cotectic high-Mg# clinopyroxene

formed, marking the transition from picritic to basaltic composition. For LT lavas (trend 2), T_p is around 1430°C (light gray circle) and fractionation is controlled by olivine, followed by plagioclase at ca. 1200°C. OIB and MORB data (open circles) are reported after Herzberg et al. (2007) and references therein; T_p calculated for other CFB provinces (open squares) are from this work.

Figure 9 – PM-Normalized incompatible element distribution of primary magmas and evolved basalts for HT2 (a) and LT (b) suites. Fractional Crystallization (FC) modelling starting from HT2 and LT primary magmas satisfactorily matches the composition of the observed differentiated basalt by removal of relative amounts of solid phases (Ol + Cpx for HT2; Ol+ Pl + Cpx for LT) obtained by major element mass balance calculation.

Figure 10 – (a) PM-Normalized trace element distribution for HT2 picrites from the Ethiopian-Yemeni CFB (shaded field), compared with high-MgO lavas from other CFB and OIB provinces. Data after Gaffney (2002); Gibson et al. (2000 and references therein); Kerr et al. (1996); Kamenetsky et al. (2012); Révillon et al. (2000); Thompson et al. (2001); Arndt et al. (1995, 1998); Carlson et al. (2006); Heinonen and Luttinen (2008 and references therein); Heinonen et al. (2010); Ellam and Cox, (1989, 1991); Melluso et al. (1995). (b) Incompatible element distribution of calculated primary HT2 picrites (shaded field) and of theoretical melts obtained by batch (F = 0.10) and fractional (F = 0.09) melting of a mantle source composed by 85% of lherzolite (xenolith GOJ40A; Beccaluva et al., 2009) and 15% of eclogite (included in Hoggar Neoproterozoic terranes; Berger et al., 2014). Source mode and melting proportions conform to experimental data by Walter (1998); partition coefficients (*Kd*) from the GERM database. Normalizing factors from Sun & McDonough (1989).

Figure 11 – Sr-Nd-Pb isotopic composition of Ethiopian-Yemeni lavas including data from Pik et al. (1999) and Teklay et al. (2005). (a) Sr-Nd isotopic composition (expressed as □(t)) of the Ethiopian-Yemeni Oligocene lavas in comparison with those recorded in other Phanerozoic CFB provinces worldwide (data from Gibson et al. 2000; Iacumin et al., 2003; Heinonen et al., 2014 and references therein; Sheth et al. 2014). (b) $^{207}Pb/^{204}Pb$ vs $^{206}Pb/^{204}Pb$ of the Ethiopian-Yemeni lavas compared with other Phanerozoic plateau basalts, MORB, OIB, geochrons and Northern Hemisphere Reference lines reported by Jackson and Carlson (2011, and references therein).

Figure 12 – $^{87}Sr/^{86}Sr$-$^{143}Nd/^{144}Nd$ (a), $^{208}Pb/^{204}Pb$-$^{206}Pb/^{204}Pb$ (b) and $^{206}Pb/^{204}Pb$-$^{87}Sr/^{86}Sr$ (c) diagrams for the Ethiopian-Yemeni CFB. Large symbols refer to data from this work, whereas small symbols to data from Pik et al. (1999) and Teklay et al. (2005). Notional mantle end-members (DM, HIMU, EMI, EMII) are after Zindler and Hart (1986) and Stracke et al. (2005). The $^{206}Pb/^{204}Pb$-$^{87}Sr/^{86}Sr$ isotopic variation observed in cpx-bulk rock pairs is shown in (d), where isotopic ratios have been recalculated for initial values at 30 Ma.

Figure 13 – TiO_2 (wt%) *vs* $^{87}Sr/^{86}Sr$ (a) and TiO_2 (wt%) *vs* $^{206}Pb/^{204}Pb$ (b) diagrams for the Ethiopian-Yemeni CFB. Large symbols refer to data from this work, whereas small symbols to data from Pik et al. (1999) and Teklay et al. (2005). Note that isotopic composition of Ethiopian CFB show a good correlation with TiO_2 content, whereas the Yemeni samples are displaced toward comparatively lower $^{87}Sr/^{86}Sr$ and higher $^{206}Pb/^{204}Pb$ isotopic values (see text for explanation).

Figure 14 – Schematic model for the generation of Oligocene Ethiopian-Yemeni CFB by the Afar plume (modified after Beccaluva et al., 2009 and updated with data from this work). The impingement of the Afar plume on the Afro-Arabian lithosphere caused regional doming and

a dramatic thermal anomaly (excess temperature T_{ex}, 300-350°C) that triggered extensive melting and eruption of CFB from the plume head. Thermo-chemical effects in the plume head progressively decreased outward as reflected by the CFB zonal arrangement with the hottest HT2 picrites (*Tp* 1570°C) at the core and LT basalts (*Tp* 1430°C) at the periphery. T_{ex} is the maximum temperature difference with respect to the ambient mantle whose temperatures are based on thermobarometric estimates of mantle xenoliths from the East-African-Arabian domain (Conticelli et al., 1998; Beccaluva et al., 2011b, Sgualdo et al., 2015). Variable amounts of eclogitic components entrained by the plume are required in the HT magma sources (up to 15% for HT2).

Seismic tomography data record a low-velocity anomaly in the upper mantle - extending for at least 1000 km from northern Ethiopia to Yemen up to *ca*. 150 km depth – that is related to the persisting effects of the Afar plume (Davaille et al., 2005; Chang and Van der Lee, 2011). See text for further explanation.

Figure 1

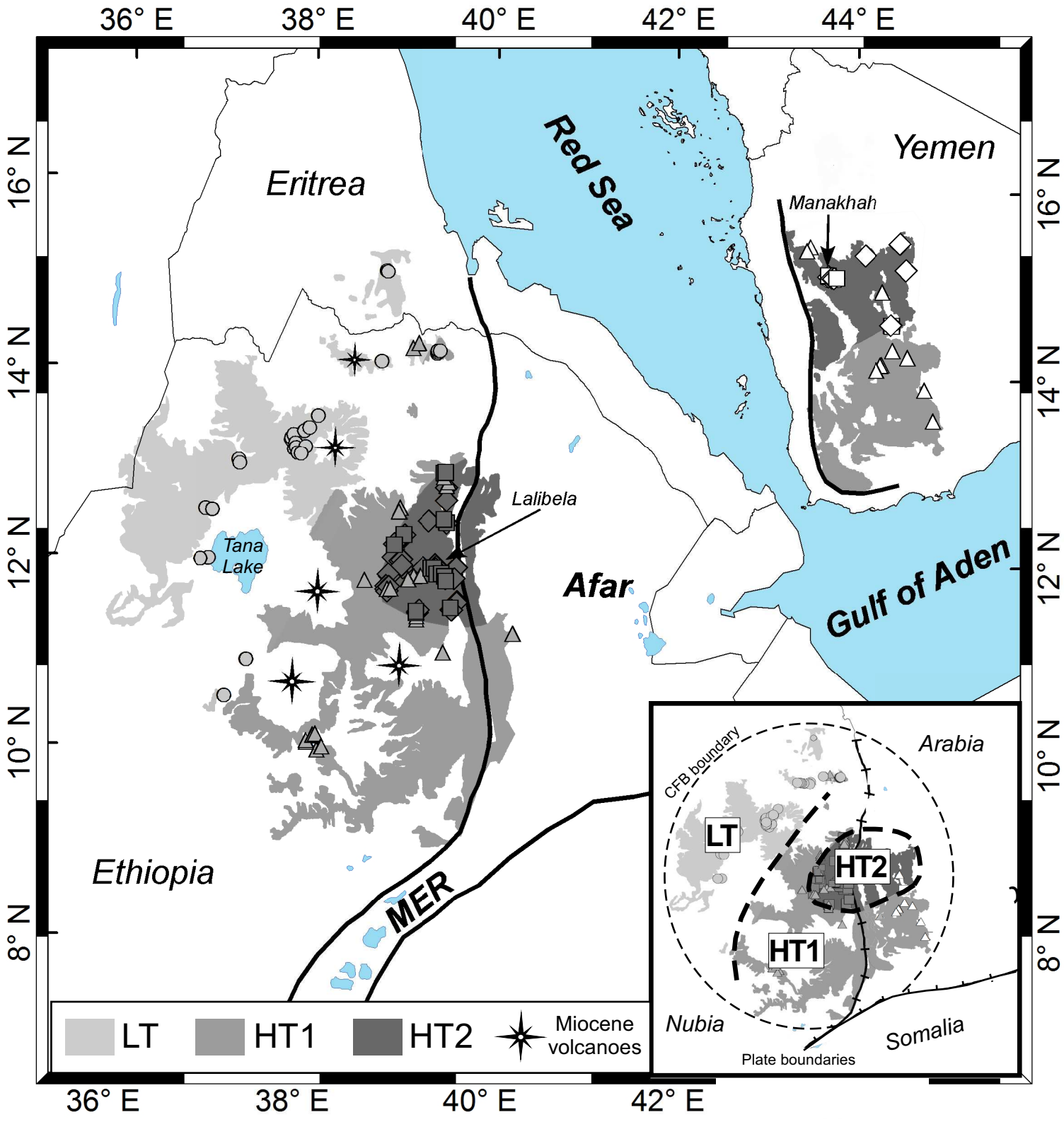
36° E
38° E
40° E
42° E
44° E
16° N
14° N
12° N
10° N
8° N
Eritrea
Red Sea
Yemen
Manakhah
Lalibela
Tana
Lake
Afar
Gulf of Aden
Ethiopia
MER
LT
HT1
HT2
Miocene
volcanoes
CFB boundary
Arabia
Nubia
Somalia
Plate boundaries

Figure 2

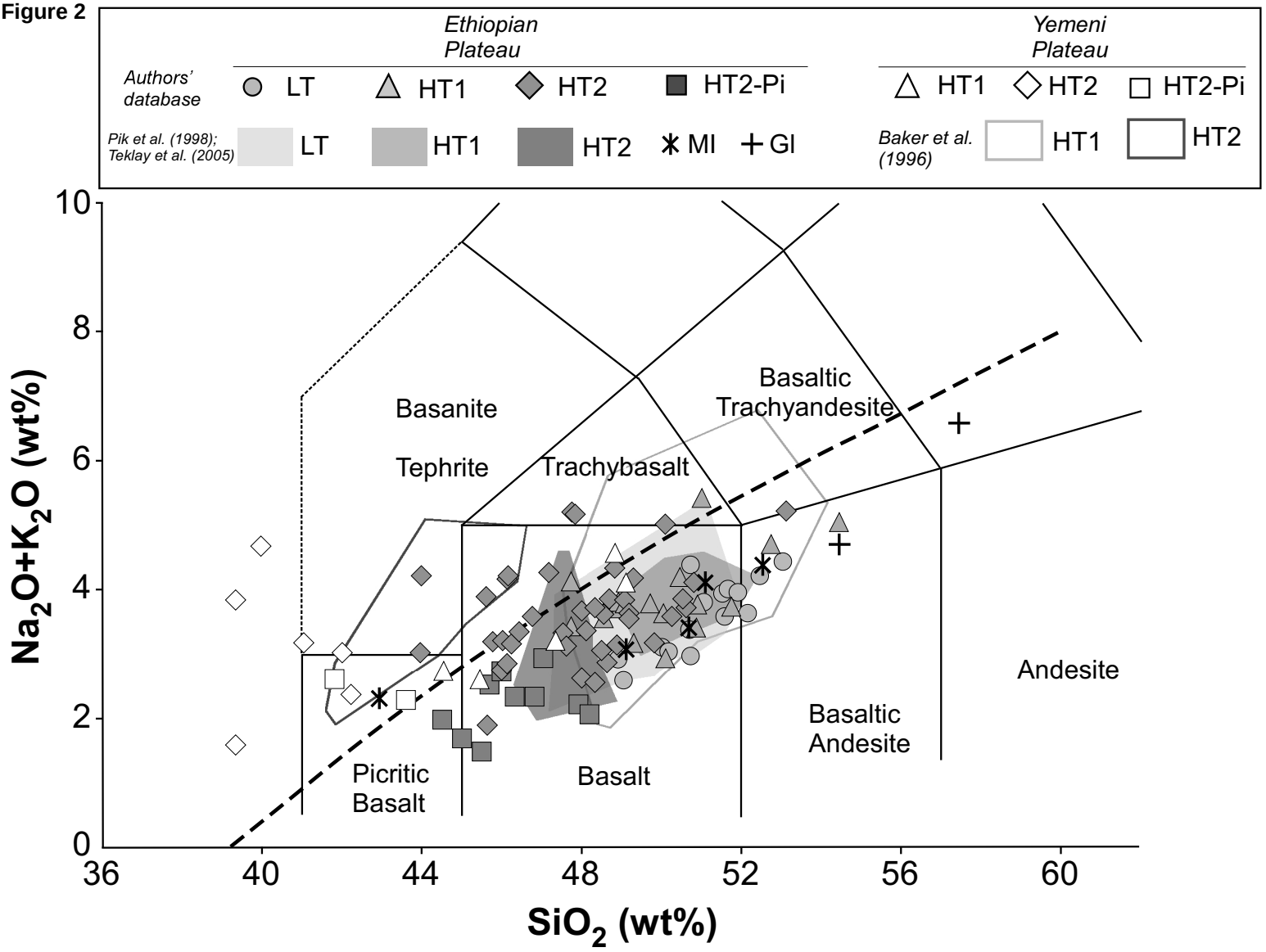
Ethiopian Plateau
Yemeni Plateau
Authors' database
LT
HT1
HT2
HT2-Pi
Pik et al. (1998); Teklay et al. (2005)
LT
HT1
HT2
MI
GI
Baker et al. (1996)
HT1
HT2
Basanite
Tephrite
Basaltic Trachyandesite
Trachybasalt
Andesite
Basaltic Andesite
Picritic Basalt
Basalt
Na_2O+K_2O (wt%)
SiO_2 (wt%)
0
2
4
6
8
10
36
40
44
48
52
56
60

Figure 3

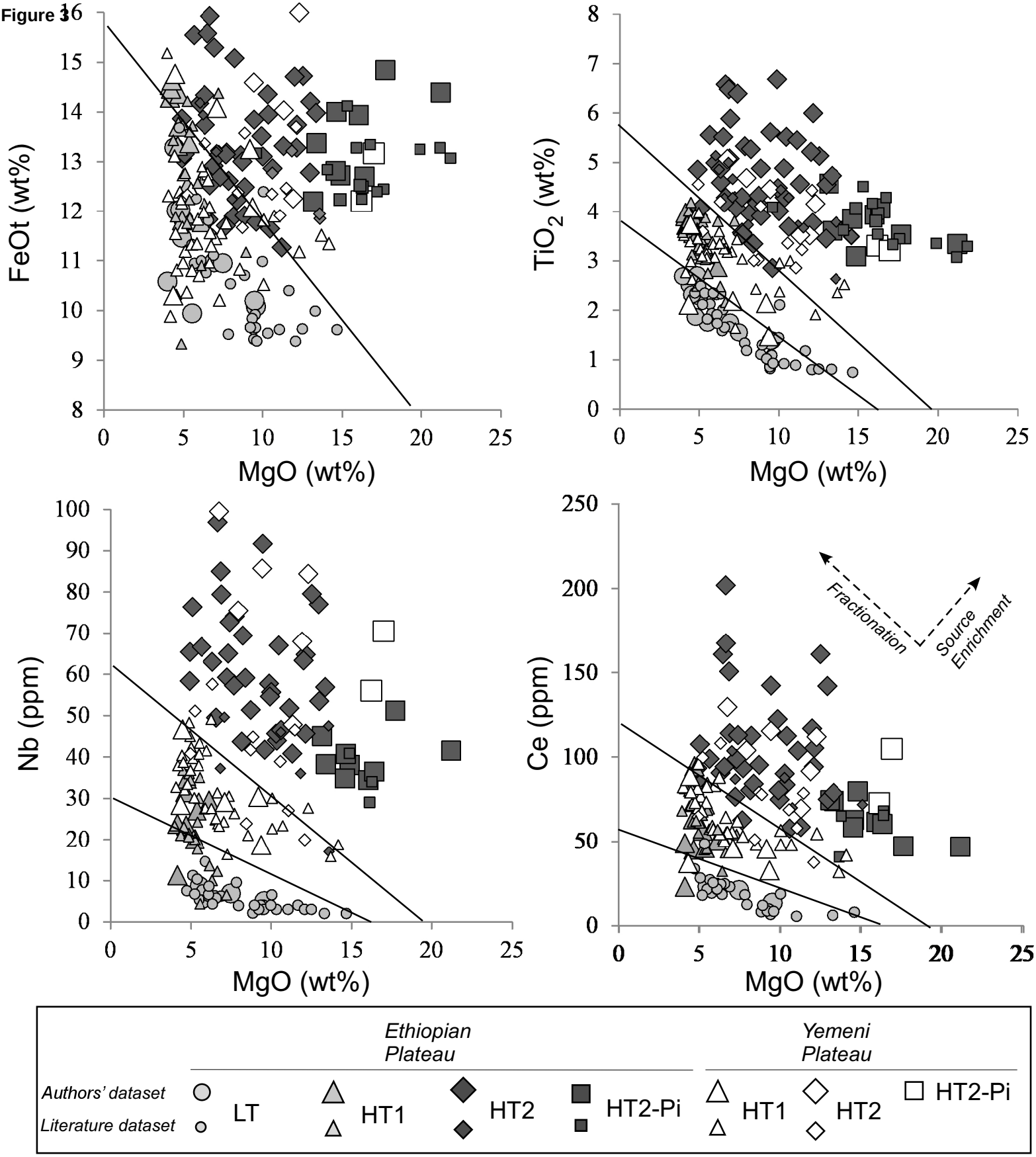
FeOt (wt%)
MgO (wt%)
TiO_2 (wt%)
MgO (wt%)
Nb (ppm)
MgO (wt%)
Ce (ppm)
MgO (wt%)
Fractionation
Source Enrichment
Ethiopian Plateau
Yemeni Plateau
Authors' dataset
Literature dataset
LT
HT1
HT2
HT2-Pi
HT1
HT2
HT2-Pi

Figure 4

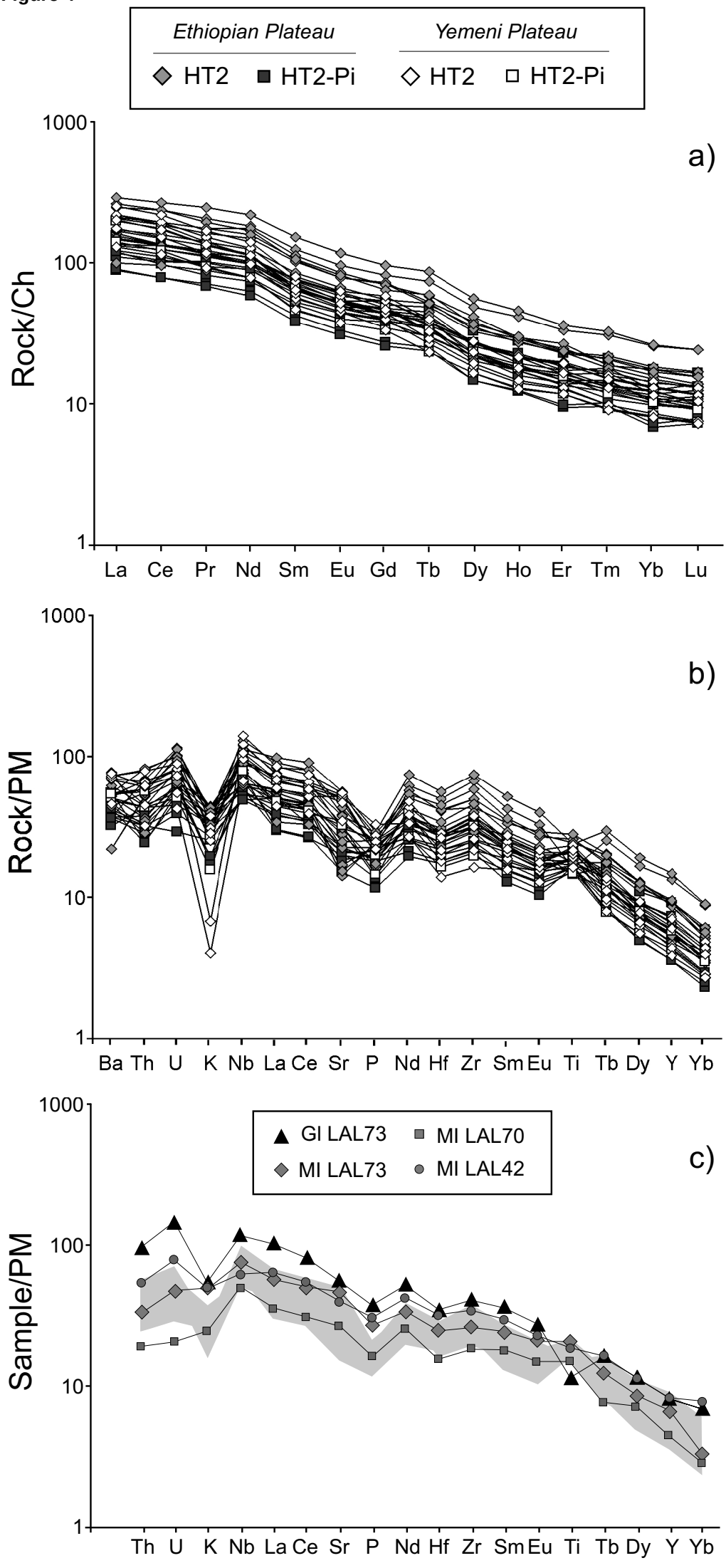
Ethiopian Plateau
Yemeni Plateau
HT2
HT2-Pi
HT2
HT2-Pi
a)
Rock/Ch
1000
100
10
1
La Ce Pr Nd Sm Eu Gd Tb Dy Ho Er Tm Yb Lu
b)
Rock/PM
1000
100
10
1
Ba Th U K Nb La Ce Sr P Nd Hf Zr Sm Eu Ti Tb Dy Y Yb
GI LAL73
MI LAL70
MI LAL73
MI LAL42
c)
Sample/PM
1000
100
10
1
Th U K Nb La Ce Sr P Nd Hf Zr Sm Eu Ti Tb Dy Y Yb

Figure 5

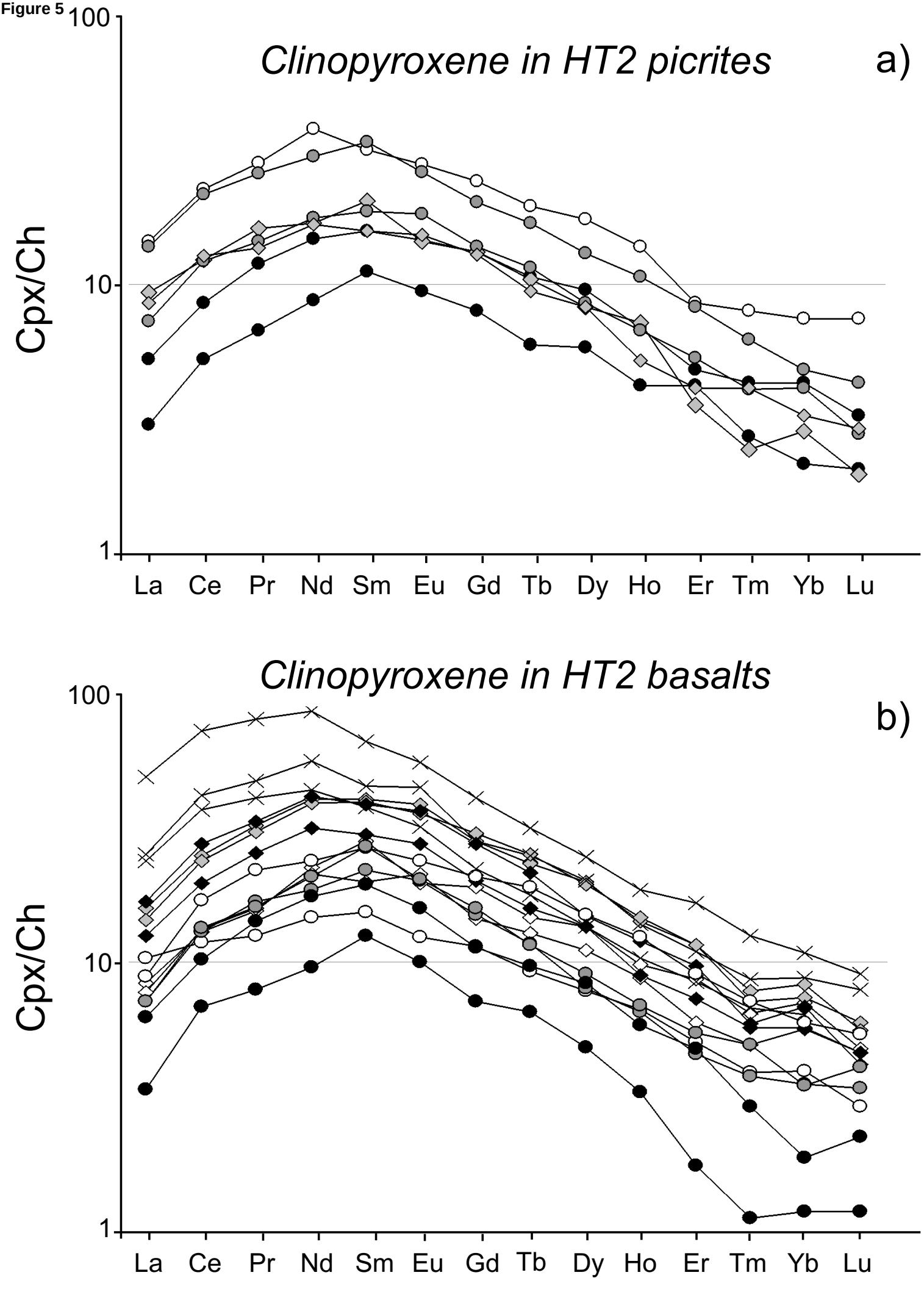
Clinopyroxene in HT2 picrites
a)
Cpx/Ch
100
10
1
La
Ce
Pr
Nd
Sm
Eu
Gd
Tb
Dy
Ho
Er
Tm
Yb
Lu
Clinopyroxene in HT2 basalts
b)
Cpx/Ch
100
10
1
La
Ce
Pr
Nd
Sm
Eu
Gd
Tb
Dy
Ho
Er
Tm
Yb
Lu

Figure 6

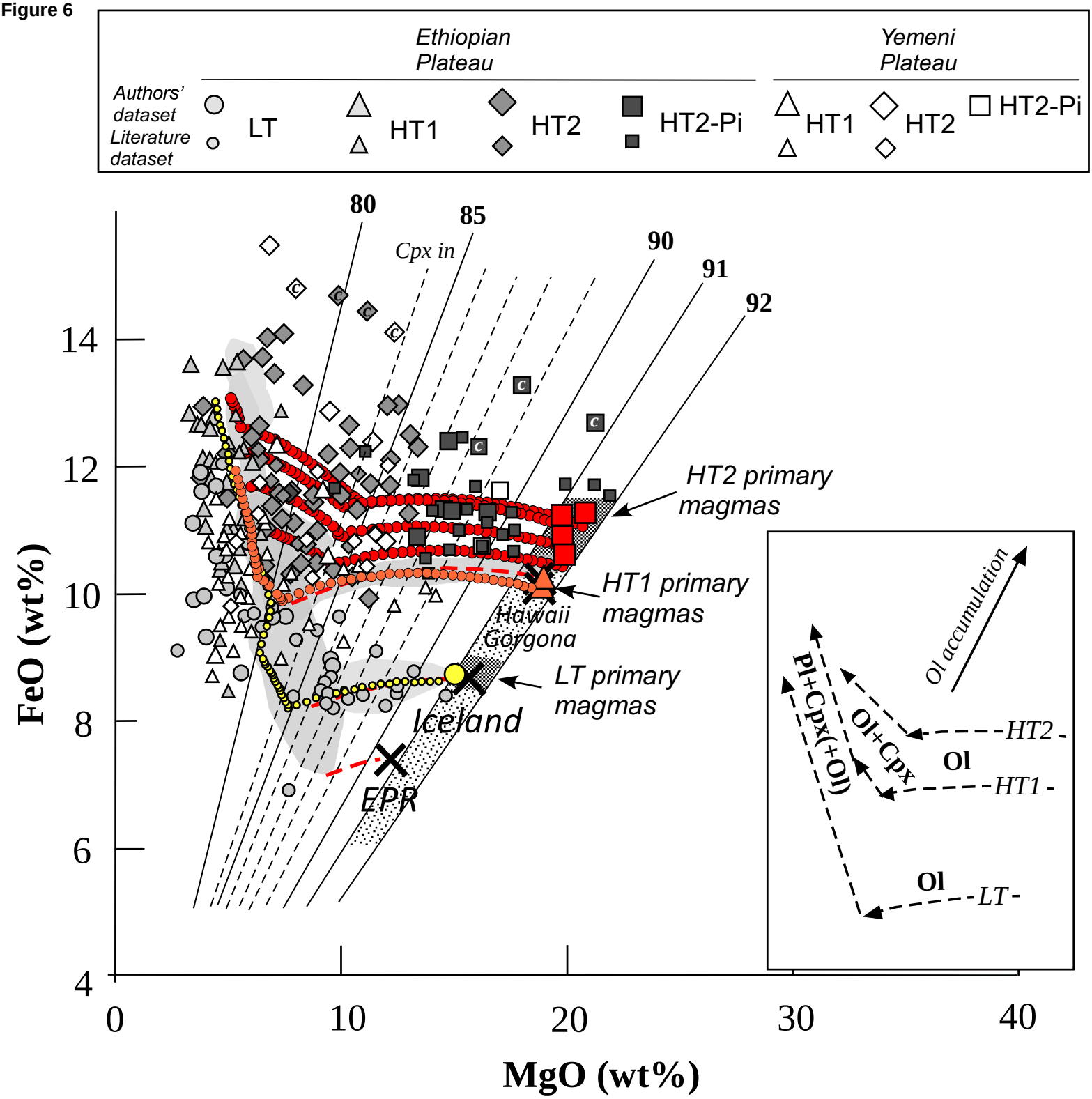
Ethiopian Plateau
Yemeni Plateau
Authors' dataset
Literature dataset
LT
HT1
HT2
HT2-Pi
HT1
HT2
HT2-Pi
80
85
90
91
92
Cpx in
HT2 primary magmas
HT1 primary magmas
Hawaii
Gorgona
LT primary magmas
Iceland
EPR
Ol accumulation
Pl+Cpx(+Ol)
Ol+Cpx
Ol
HT2
HT1
Ol
LT
FeO (wt%)
MgO (wt%)
14
12
10
8
6
4
0
10
20
30
40

Figure 7

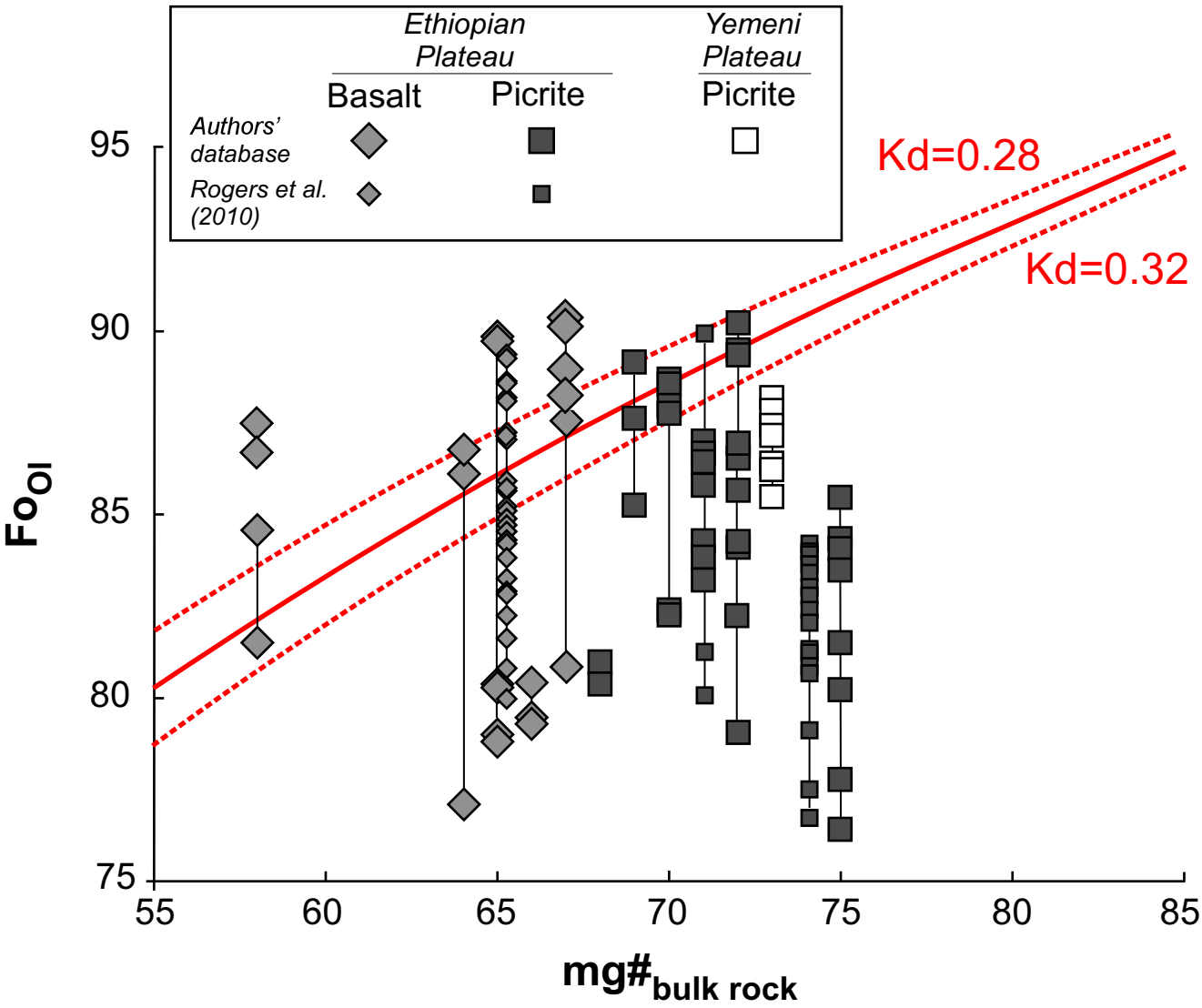
Ethiopian Plateau
Yemeni Plateau
Basalt
Picrite
Picrite
Authors' database
Rogers et al. (2010)
Kd=0.28
Kd=0.32
95
90
85
80
75
55
60
65
70
75
80
85
Fo_OI
mg#_bulk rock

Figure 8

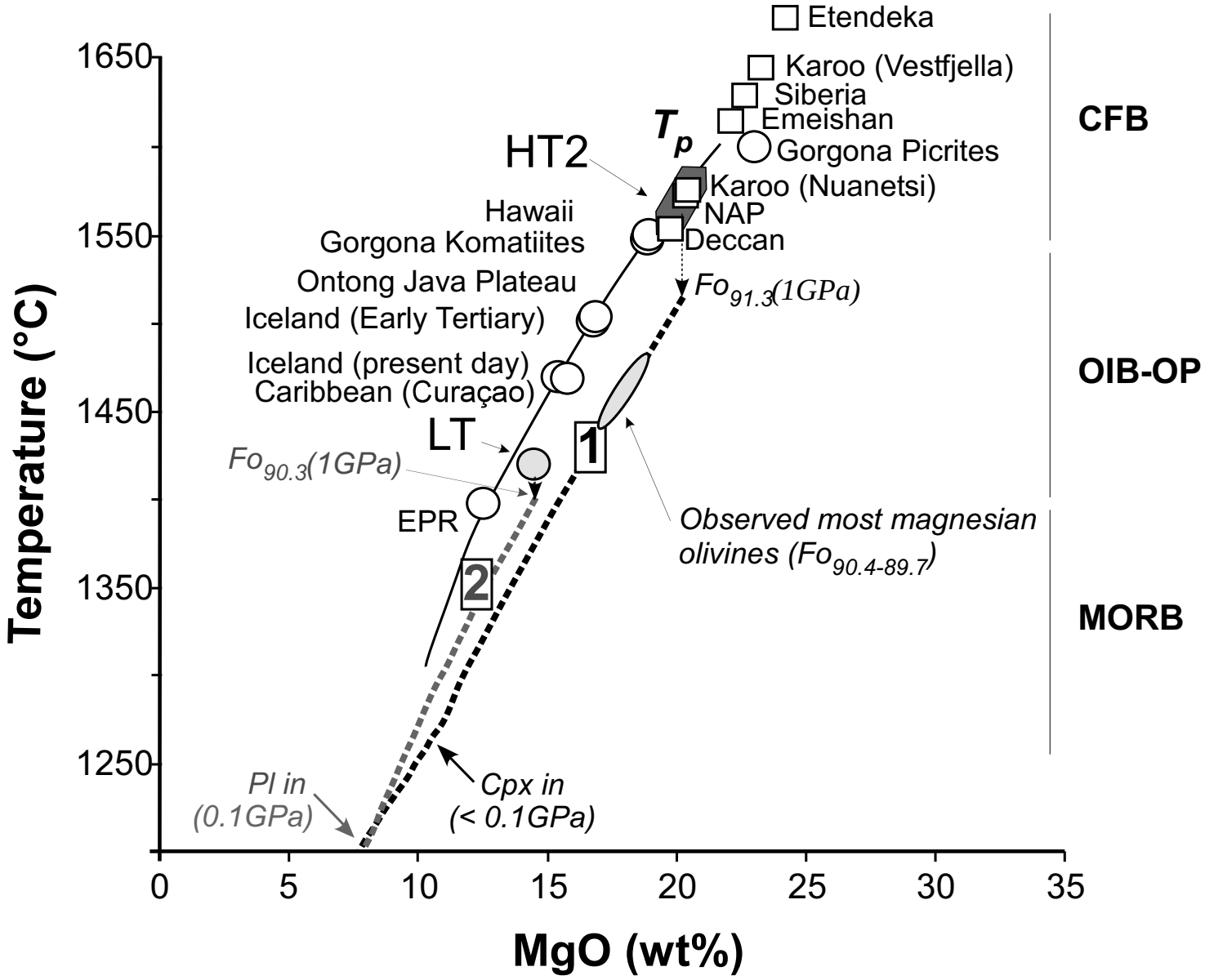
Etendeka
Karoo (Vestfjella)
Siberia
Emeishan
Gorgona Picrites
Karoo (Nuanetsi)
NAP
Deccan
Hawaii
Gorgona Komatiites
Ontong Java Plateau
Iceland (Early Tertiary)
Iceland (present day)
Caribbean (Curaçao)
HT2
T_p
LT
EPR
1
2
$Fo_{91.3}$(1GPa)
$Fo_{90.3}$(1GPa)
Observed most magnesian olivines ($Fo_{90.4-89.7}$)
Pl in (0.1GPa)
Cpx in (< 0.1GPa)
CFB
OIB-OP
MORB
Temperature (°C)
MgO (wt%)
1650
1550
1450
1350
1250
0
5
10
15
20
25
30
35

Figure 9

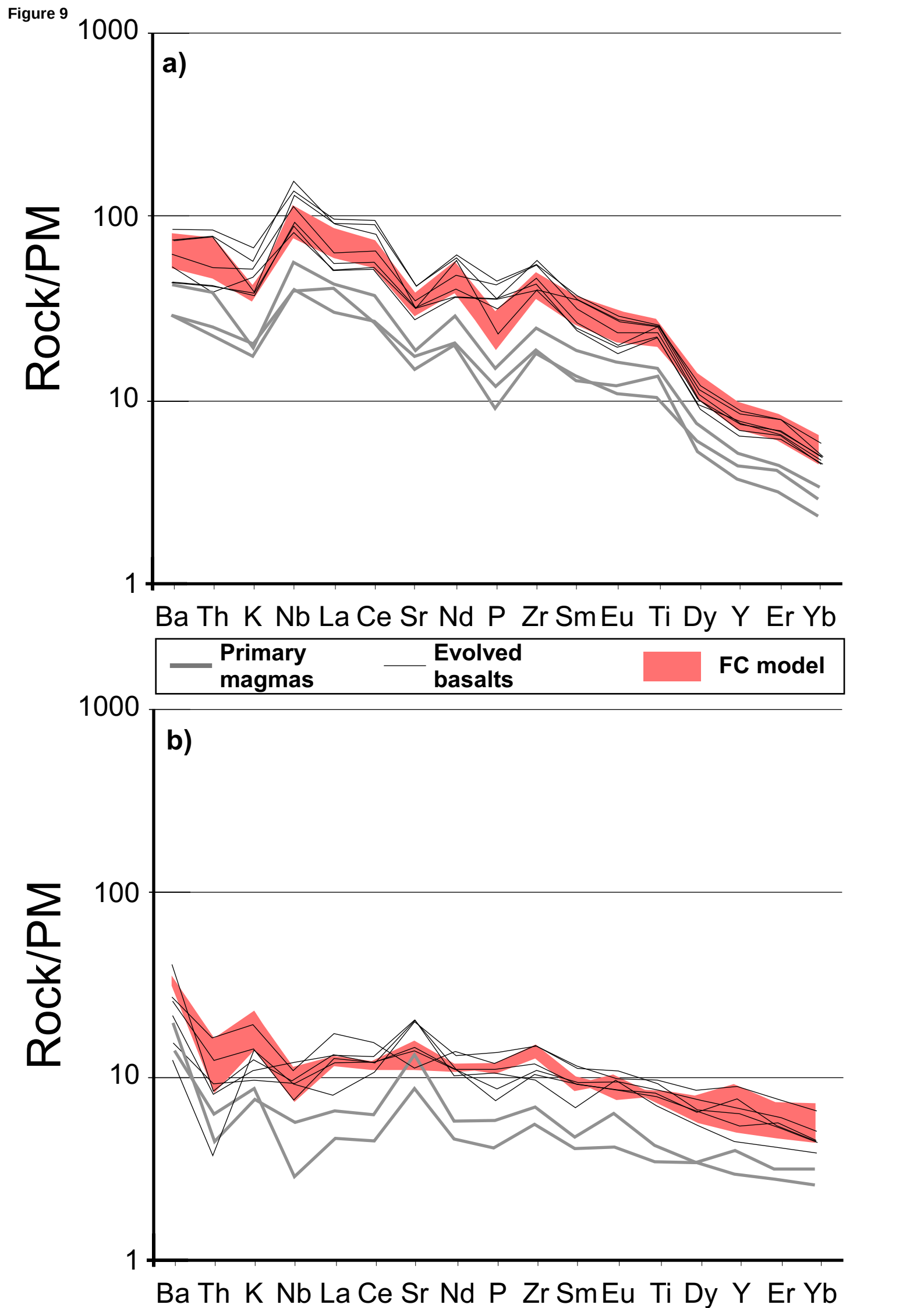
a)
1000
100
10
1
Rock/PM
Ba Th K Nb La Ce Sr Nd P Zr Sm Eu Ti Dy Y Er Yb
Primary magmas
Evolved basalts
FC model
b)
1000
100
10
1
Rock/PM
Ba Th K Nb La Ce Sr Nd P Zr Sm Eu Ti Dy Y Er Yb

Figure 10

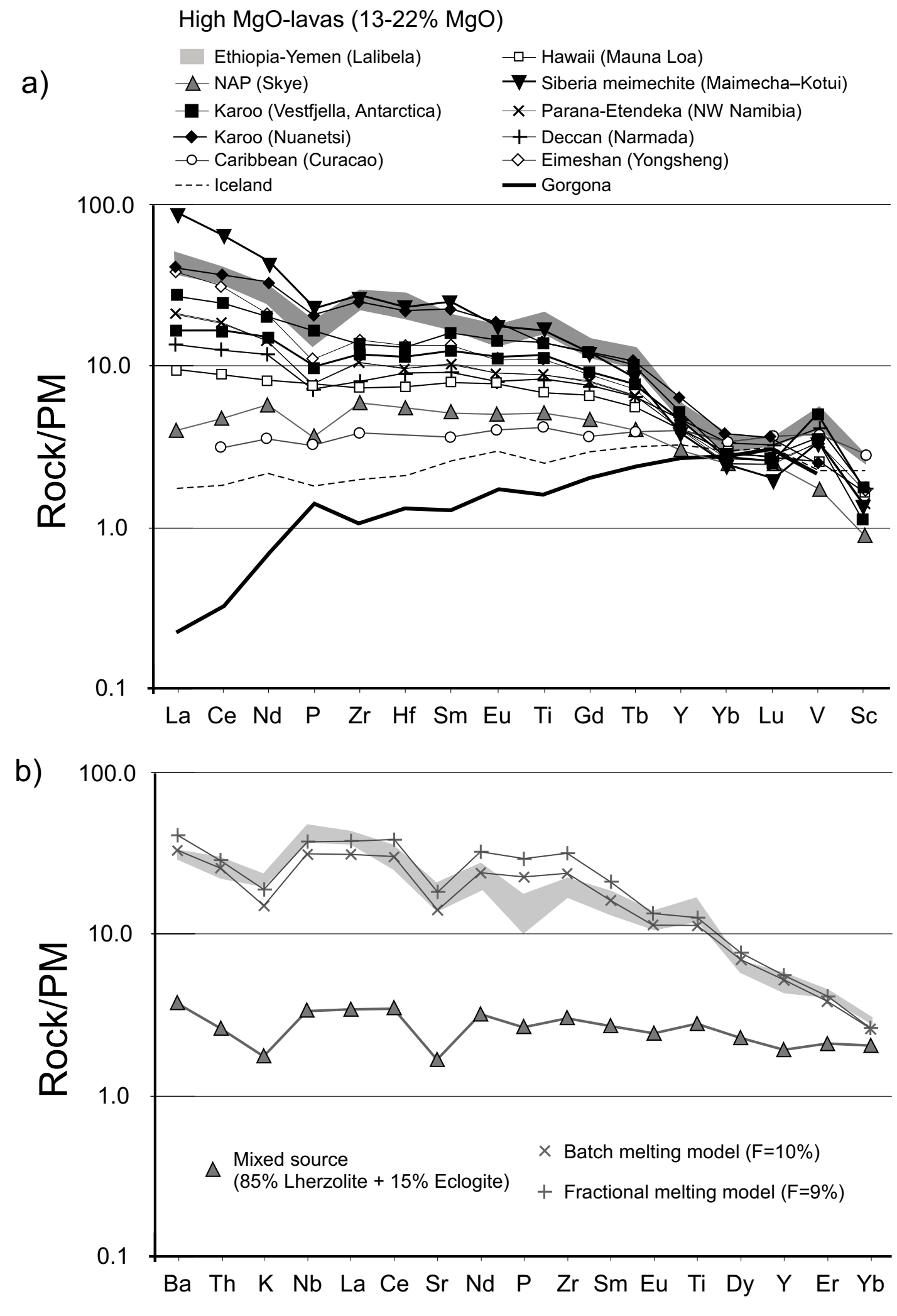
High MgO-lavas (13-22% MgO)
a)
Ethiopia-Yemen (Lalibela)
NAP (Skye)
Karoo (Vestfjella, Antarctica)
Karoo (Nuanetsi)
Caribbean (Curacao)
Iceland
Hawaii (Mauna Loa)
Siberia meimechite (Maimecha–Kotui)
Parana-Etendeka (NW Namibia)
Deccan (Narmada)
Eimeshan (Yongsheng)
Gorgona
Rock/PM
100.0
10.0
1.0
0.1
La Ce Nd P Zr Hf Sm Eu Ti Gd Tb Y Yb Lu V Sc
b)
Rock/PM
100.0
10.0
1.0
0.1
Mixed source
(85% Lherzolite + 15% Eclogite)
Batch melting model (F=10%)
Fractional melting model (F=9%)
Ba Th K Nb La Ce Sr Nd P Zr Sm Eu Ti Dy Y Er Yb

Figure 11

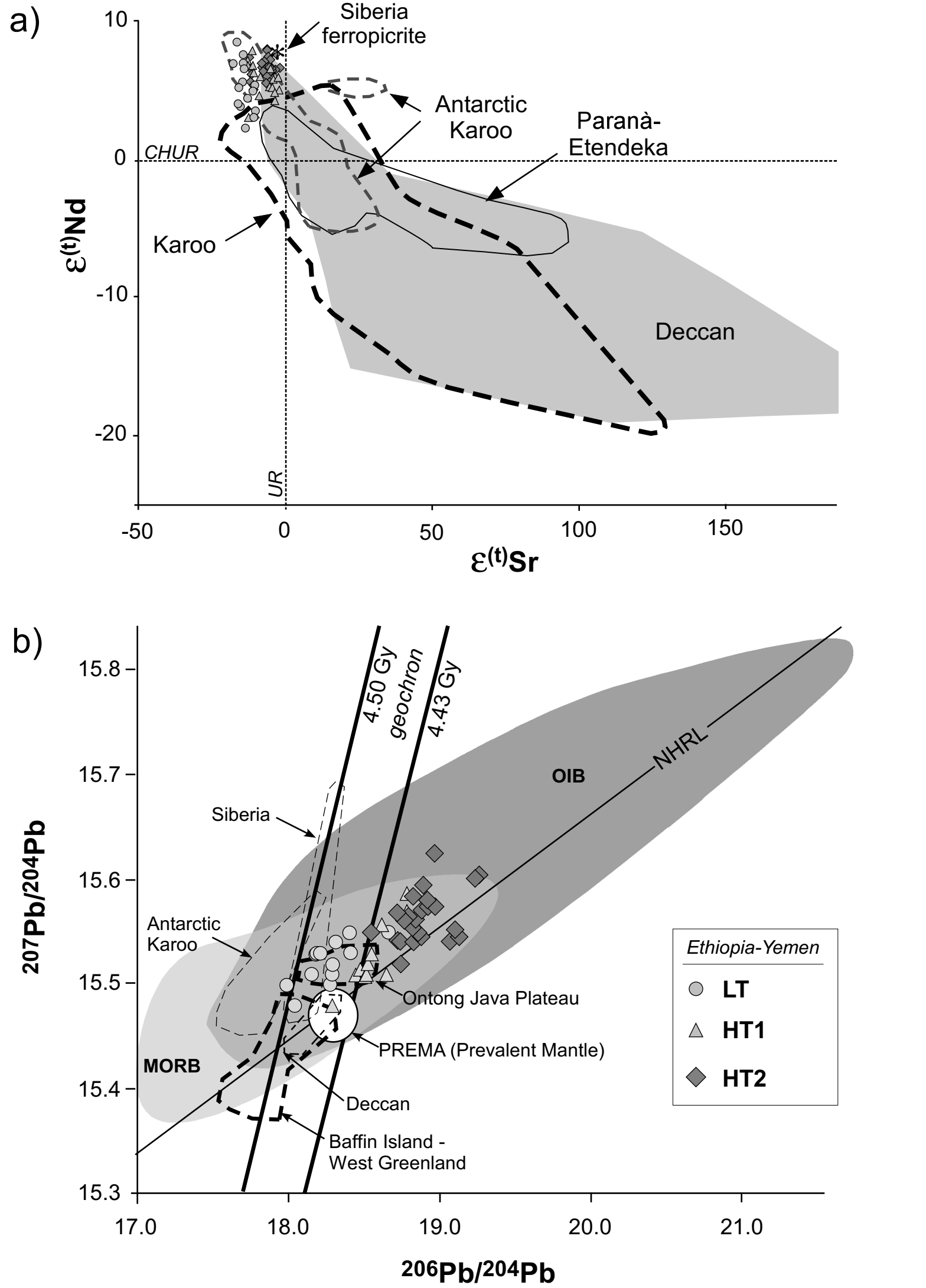
a)
Siberia
ferropicrite
Antarctic
Karoo
Paranà-
Etendeka
CHUR
Karoo
Deccan
UR
10
0
-10
-20
-50
0
50
100
150
ε(t)Nd
ε(t)Sr
b)
4.50 Gy
geochron
4.43 Gy
NHRL
OIB
Siberia
Antarctic
Karoo
Ontong Java Plateau
PREMA (Prevalent Mantle)
MORB
Deccan
Baffin Island -
West Greenland
Ethiopia-Yemen
LT
HT1
HT2
15.8
15.7
15.6
15.5
15.4
15.3
17.0
18.0
19.0
20.0
21.0
207Pb/204Pb
206Pb/204Pb

Figure 12

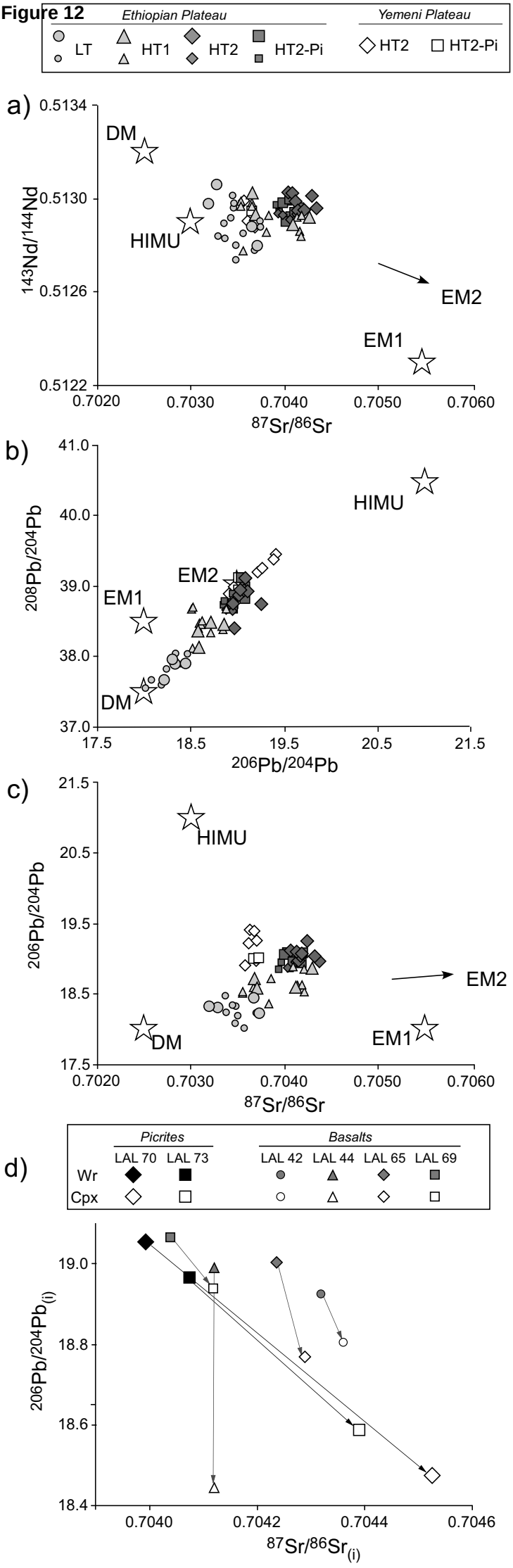
Ethiopian Plateau
Yemeni Plateau
LT
HT1
HT2
HT2-Pi
HT2
HT2-Pi
a)
DM
HIMU
EM2
EM1
143Nd/144Nd
87Sr/86Sr
b)
HIMU
EM2
EM1
DM
208Pb/204Pb
206Pb/204Pb
c)
HIMU
EM2
DM
EM1
206Pb/204Pb
87Sr/86Sr
d)
Picrites
Basalts
LAL 70
LAL 73
LAL 42
LAL 44
LAL 65
LAL 69
Wr
Cpx
206Pb/204Pb(i)
87Sr/86Sr(i)

Figure 13

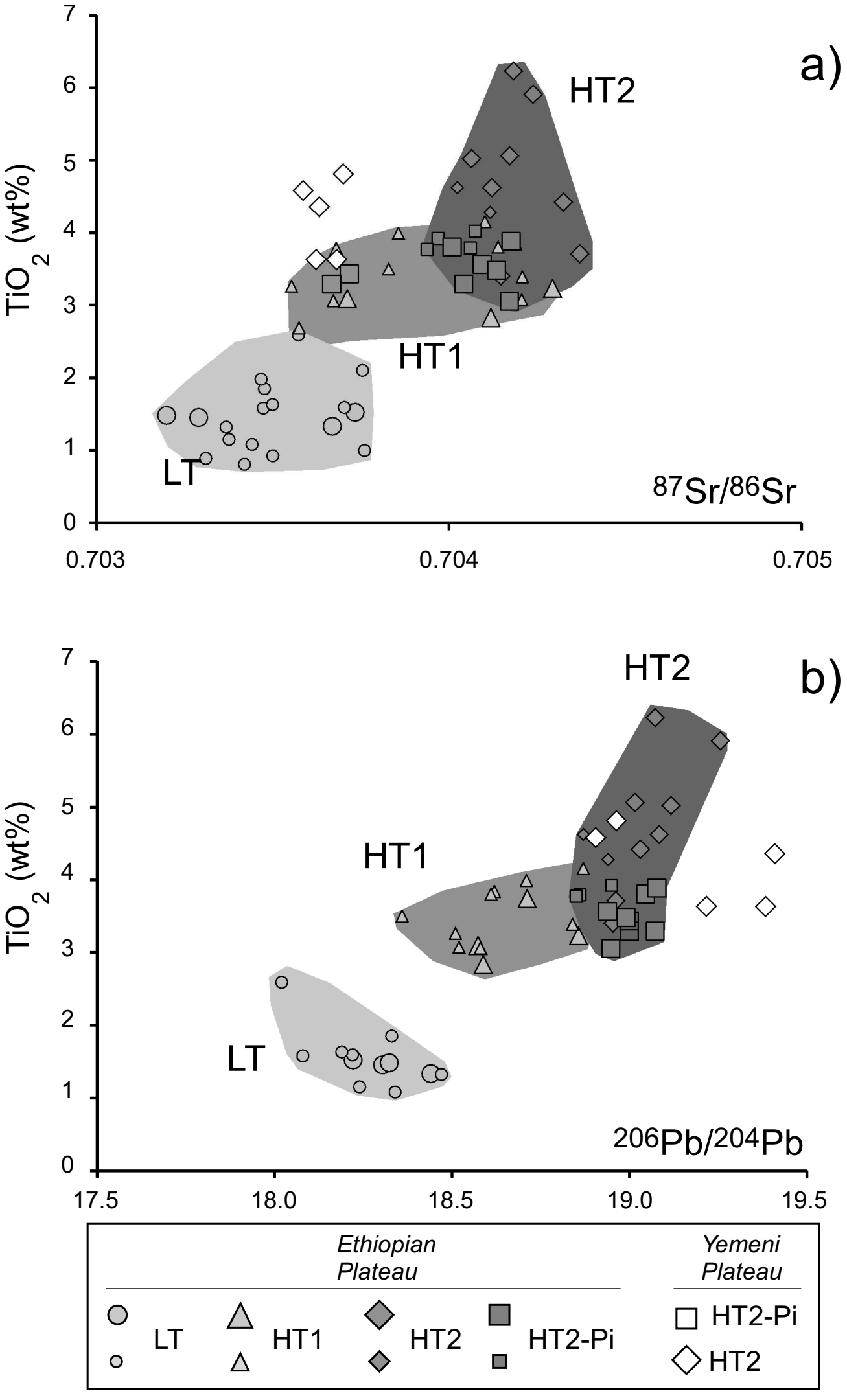
a)
HT2
HT1
LT
TiO_2 (wt%)
$^{87}Sr/^{86}Sr$
0.703
0.704
0.705
b)
HT2
HT1
LT
TiO_2 (wt%)
$^{206}Pb/^{204}Pb$
17.5
18.0
18.5
19.0
19.5
Ethiopian Plateau
Yemeni Plateau
LT
HT1
HT2
HT2-Pi
HT2-Pi
HT2

Figure 14

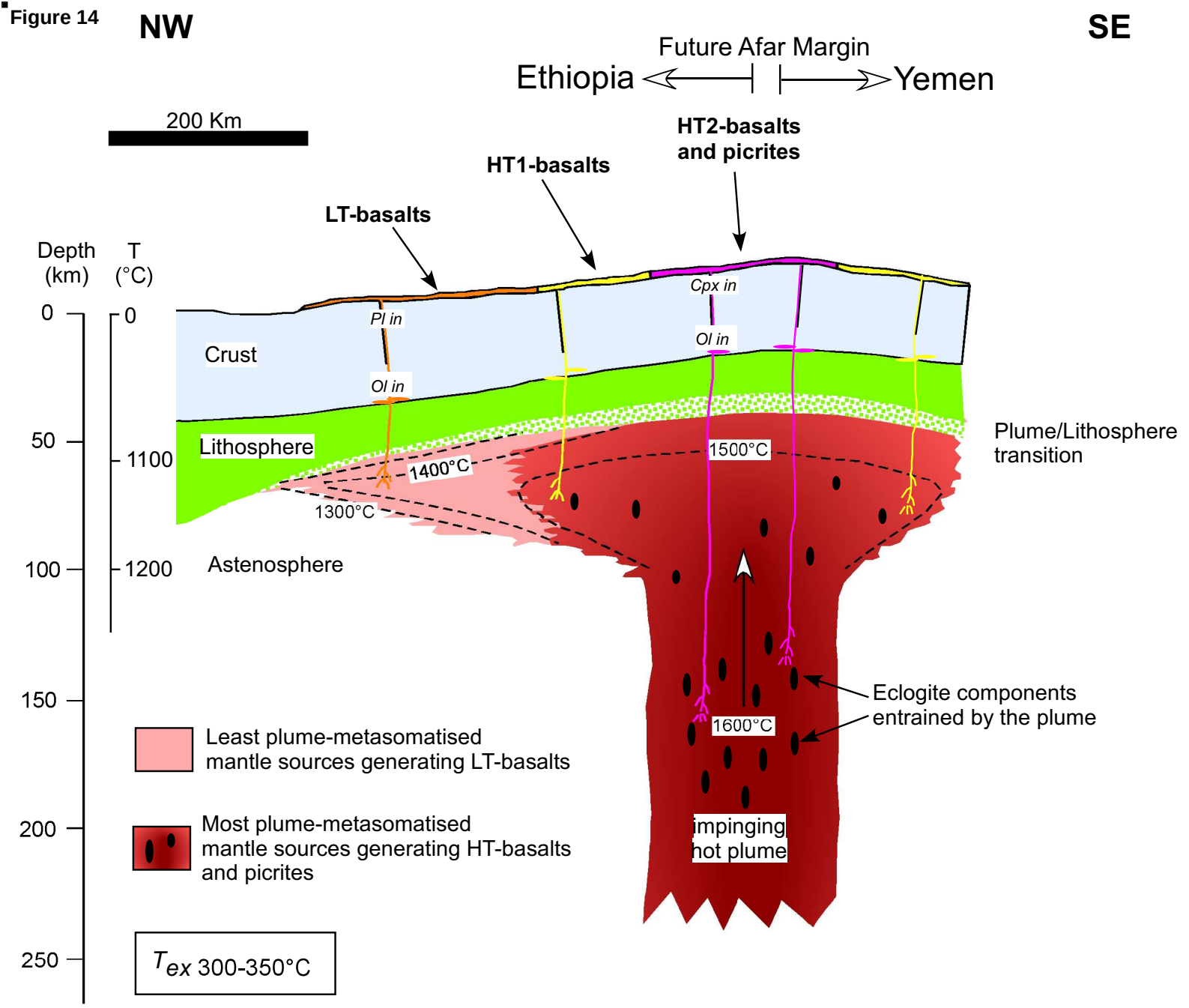
NW
SE
Future Afar Margin
Ethiopia
Yemen
200 Km
HT2-basalts
and picrites
HT1-basalts
LT-basalts
Depth
(km)
T
(°C)
0
0
Pl in
Cpx in
Ol in
Crust
Ol in
50
1100
Lithosphere
1400°C
1500°C
1300°C
Plume/Lithosphere
transition
100
1200
Astenosphere
150
Eclogite components
entrained by the plume
1600°C
Least plume-metasomatised
mantle sources generating LT-basalts
200
Most plume-metasomatised
mantle sources generating HT-basalts
and picrites
impinging
hot plume
250
T_{ex} 300-350°C

Table 1

Table 1

Ethiopian plateau (Lalibela suite)

Rock type	Picrite									Basalt												
Lon. *(dd)*	39.4200	39.4056	39.3950	39.2403	39.5544	39.4617	39.4308	39.5433	39.5217	39.5156	39.4275	39.0039	38.9861	39.2375	39.5514	39.5411	39.5003	39.0100	39.5478	39.5431	39.5297	39.5469
Lat.	11.9664	11.9536	11.9442	11.4878	11.8242	11.8956	11.9464	12.4431	12.4742	11.8869	11.9742	11.9450	11.9336	11.4781	11.8458	11.8706	11.8892	12.2181	12.4350	12.4428	12.4561	12.8128
Sample	**LAL5***	**LAL6***	**LAL9***	**LAL33**	**LAL41**	**LAL45**	**LAL47***	**LAL70**	**LAL73***	**LAL1***	**LAL3***	**LAL14***	**LAL15***	**LAL31**	**LAL42**	**LAL43**	**LAL44**	**LAL60***	**LAL65**	**LAL69**	**LAL72***	**LAL76***
SiO_2 *(wt%)*	46.57	45.66	46.83	47.79	48.15	45.77	46.26	44.52	44.36	48.06	50.60	46.26	45.84	48.55	48.14	45.64	45.41	47.21	45.80	45.75	48.12	48.92
TiO_2	4.57	4.07	3.49	3.61	3.09	3.86	3.93	3.34	3.53	5.50	3.97	5.99	5.57	3.44	3.76	5.09	5.13	4.85	4.48	4.68	4.44	3.69
Al_2O_3	8.69	8.40	8.87	8.99	8.30	8.62	7.79	6.02	6.87	8.14	11.12	7.88	9.34	9.22	9.57	7.95	8.35	8.51	8.10	7.48	8.87	9.99
FeO	10.75	11.19	11.29	11.78	11.21	12.34	12.28	12.68	13.07	10.23	10.47	12.09	12.10	11.22	11.63	12.87	12.76	12.55	12.31	12.19	11.79	11.32
Fe_2O_3	1.61	1.68	1.69	1.77	1.68	1.85	1.84	1.90	1.96	1.53	1.57	1.81	1.81	1.68	1.74	1.93	1.91	1.88	1.85	1.83	1.77	1.70
MnO	0.20	0.18	0.18	0.18	0.18	0.18	0.17	0.18	0.18	0.17	0.17	0.17	0.19	0.18	0.17	0.17	0.16	0.17	0.16	0.17	0.17	0.17
MgO	13.16	16.40	14.59	13.39	14.89	14.64	16.04	21.21	17.70	10.43	8.17	12.13	9.40	12.92	12.06	12.44	11.83	10.24	12.78	13.22	9.84	10.61
CaO	10.15	9.37	10.41	9.58	9.97	9.15	8.74	7.79	8.89	11.81	9.85	9.96	10.46	9.20	9.57	9.94	9.35	10.19	9.26	10.48	10.62	9.97
Na_2O	1.92	1.75	1.55	1.65	1.53	1.63	1.44	0.98	1.10	2.02	2.43	1.98	2.95	1.84	1.69	1.53	1.88	2.15	2.11	1.87	1.84	2.06
K_2O	0.97	0.75	0.80	0.57	0.54	1.10	0.89	0.98	0.57	1.31	1.28	1.18	1.19	1.01	0.85	1.19	1.27	1.16	1.17	0.96	1.20	1.09
P_2O_5	0.41	0.40	0.29	0.40	0.30	0.46	0.44	0.39	0.25	0.61	0.36	0.53	0.50	0.53	0.37	0.63	0.55	0.48	0.52	0.50	0.55	0.49
LOI	1.01	0.16	0.00	0.30	0.16	0.42	0.17	0.00	1.51	0.16	0.00	0.02	0.65	0.20	0.45	0.63	1.40	0.62	1.46	0.85	0.80	0.00
mg#	0.69	0.72	0.70	0.67	0.70	0.68	0.70	0.75	0.71	0.65	0.58	0.64	0.58	0.67	0.65	0.63	0.62	0.59	0.65	0.66	0.60	0.63
Ni *(ppm)*	646	1097	697	509	569	565	724	984	836	237	233	611	214	481	439	318	385	168	434	411	212	327
Co	67	71	71	76	80	77	92	106	92	45	48	59	56	73	69	76	74	64	71	73	66	65
Cr	808	1551	1203	899	1348	995	1100	1820	1240	595	494	814	478	859	817	625	583	433	976	1022	528	723
V	449	371	343	360	345	345	343	305	356	475	400	482	513	343	353	386	399	442	367	390	383	361
Sc	44	43	43	40	41	37	38	36	33	53	41	50	43	40	38	51	43	46	38	45	48	38
Rb	15	5	7	15	28	26	19	22	24	15	20	19	20	23	21	23	26	28	28	31	20	23
Sr	457	470	392	435	396	460	442	555	454	596	516	684	673	407	496	678	608	672	389	457	570	471
Ba	336	259	253	258	225	288	276	383	292	377	426	369	507	258	305	385	365	428	359	535	381	310
Zr	309	265	249	315	240	342	356	288	282	436	320	495	442	307	329	499	510	478	428	434	406	316
Hf	8.72	6.68	6.15	8.26	8.63	7.40	7.54	5.53	5.30	12.8	8.17	12.9	12.5	15.3	10.5	17.3	13.9	8.83	8.31	8.23	9.45	7.06
Nb	45.0	36.5	34.8	38.2	38.1	40.8	34.4	41.5	51.2	67.0	43.7	64.8	91.7	77.0	45.6	79.5	63.4	45.6	53.5	56.9	54.6	46.5
Ta	2.66	2.10	2.11	1.38	1.39	1.43	1.26	2.41	2.93	4.03	2.68	4.39	7.10	2.61	1.65	2.79	2.28	1.66	3.10	3.34	3.27	2.72
Th	3.68	2.72	2.41	3.17	3.67	2.80	2.72	2.08	2.05	4.37	4.48	5.71	6.73	5.78	4.61	6.95	4.93	3.74	3.06	2.92	4.92	2.43
U	0.93	0.60	0.81	1.30	1.28	1.25	1.13	1.03	1.14	1.39	1.59	1.64	2.11	2.42	2.08	2.10	1.97	1.68	1.38	1.18	2.35	1.32
Y	26.4	21.4	25.1	33.2	41.3	23.6	24.7	16.1	16.2	41.8	30.0	39.2	39.7	60.1	42.0	67.3	42.8	52.6	28.0	24.4	50.1	41.6
La	33.2	26.1	*35.0***	30.8	34.0	27.3	25.7	20.4	20.8	47.5	37.7	45.2	61.2	57.5	40.0	67.4	49.2	39.0	30.7	31.2	34.5	23.3
Ce	74.5	60.3	58.3	74.0	79.6	62.7	61.5	46.7	47.1	113	80.5	105	142	142	94.4	161	117	90.2	75.0	78.9	80.4	57.7
Pr	11.0	8.8	7.57	10.3	11.3	9.5	9.2	6.6	6.3	15.16	10.74	16.2	18.2	19.2	13.2	22.9	16.4	12.3	10.5	10.8	11.4	8.20
Nd	43.5	35.0	33.9	45.0	49.7	42.0	40.9	28.7	26.4	68.9	45.1	68.0	77.6	83.5	57.2	101	72.7	51.4	46.2	46.7	50.1	35.7
Sm	9.30	7.40	7.63	10.0	11.6	9.5	9.1	6.3	5.7	15.3	9.64	14.7	15.5	18.6	12.9	23.0	16.1	10.3	10.5	10.1	11.2	7.96
Eu	3.05	2.55	2.27	2.98	3.48	3.05	2.69	1.90	1.74	4.45	2.79	4.83	4.50	5.47	3.81	6.64	4.66	2.89	3.13	2.96	3.44	2.49
Gd	8.73	6.93	7.65	8.94	10.3	10.8	8.15	5.52	5.18	14.6	9.52	13.8	14.5	16.4	11.1	19.3	13.1	7.91	9.27	8.72	9.61	7.86
Tb	1.40	1.13	1.07	1.49	1.78	1.44	1.29	0.91	0.87	1.95	1.31	2.18	1.85	2.72	1.91	3.20	2.16	1.26	1.56	1.43	1.64	1.24
Dy	6.23	5.00	5.47	6.63	8.11	5.57	5.37	3.68	3.61	9.46	6.62	9.43	8.87	12.1	8.51	13.9	9.23	5.30	6.34	5.74	6.64	5.01
Ho	1.11	0.90	0.97	1.25	1.54	1.01	1.02	0.68	0.69	1.59	1.17	1.69	1.50	2.29	1.60	2.54	1.67	0.95	1.19	1.06	1.24	0.96
Er	2.40	1.94	2.51	2.97	3.68	2.61	2.39	1.54	1.59	4.01	3.06	3.68	3.79	5.44	3.80	5.87	3.85	2.21	2.64	2.36	2.77	2.25
Tm	0.38	0.30	0.31	0.42	0.52	0.33	0.32	0.24	0.25	0.47	0.38	0.52	0.44	0.77	0.54	0.81	0.52	0.31	0.42	0.36	0.45	0.36
Yb	1.84	1.46	1.79	2.36	2.93	2.03	1.83	1.14	1.22	2.64	2.19	2.63	2.50	4.30	3.01	4.39	2.81	1.68	1.97	1.71	2.09	1.77
Lu	0.26	0.25	0.24	0.33	0.41	0.26	0.24	0.18	0.19	0.34	0.29	0.42	0.33	0.60	0.42	0.61	0.38	0.24	0.31	0.27	0.34	0.28

Table 1 – *(continued)*

Yemeni plateau (Manakhah suite)

Rock type	Picrite		Basalt					
Lon. *(dd)*	43.7278	43.7111	43.7347	43.7325	43.7292	43.7247	43.7247	43.7278
Lat.	15.0881	15.1028	15.0953	15.0881	15.0828	15.0900	15.0900	15.0881
Sample	**YE26**	**YE29**	**YE23**	**YE24**	**YE25**	**YE27**	**YE28**	**YE31**
SiO_2 *(wt%)*	42.22	40.93	37.86	39.20	41.20	38.15	40.31	40.98
TiO_2	3.31	3.21	4.16	4.46	3.52	5.07	4.69	3.52
Al_2O_3	9.98	9.90	9.55	13.25	11.20	11.76	12.10	12.33
FeO	10.75	11.60	14.09	12.86	12.37	15.41	14.78	10.80
Fe_2O_3	1.61	1.74	2.11	1.93	1.85	2.31	2.22	1.62
MnO	0.20	0.19	0.23	0.21	0.20	0.21	0.20	0.17
MgO	16.21	16.98	12.30	9.46	11.34	6.77	7.96	11.93
CaO	9.98	10.38	13.93	11.49	13.10	13.00	12.31	12.48
Na_2O	1.74	1.74	1.32	3.81	2.20	2.80	2.26	1.81
K_2O	0.47	0.81	0.20	0.76	0.12	0.92	0.85	1.13
P_2O_5	0.31	0.43	0.46	0.60	0.47	0.54	0.47	0.71
LOI	3.21	2.09	3.77	1.98	2.42	3.05	1.84	2.52
mg#	0.73	0.72	0.61	0.57	0.62	0.44	0.49	0.66
Ni *(ppm)*	520	363	214	54	167	1	41	99
Co	65	59	68	47	63	56	55	55
Cr	935	673	540	19	556	23	118	279
V	367	363	521	382	400	522	517	379
Sc	33	32	54	39	43	53	49	35
Rb	7	38	3	7	nd	20	14	27
Sr	671	1071	1065	1106	724	1158	989	1087
Ba	356	377	478	481	321	500	526	493
Zr	217	361	281	420	183	349	288	238
Hf	4.98	8.07	6.14	8.84	4.26	8.02	6.66	5.51
Nb	56.0	70.5	84.4	85.6	47.8	99.5	75.5	67.9
Ta	3.74	4.57	5.24	5.46	3.17	6.35	4.84	4.33
Th	3.65	4.72	5.14	5.51	2.69	6.63	5.20	3.80
U	1.05	1.50	1.70	1.72	0.88	1.86	1.51	1.15
Y	19.3	26.1	19.7	33.5	17.6	31.8	27.4	20.8
La	32.8	46.2	51.2	50.4	30.1	58.7	46.8	40.5
Ce	72.7	105	112	116	69.6	130	104	91.6
Pr	8.74	12.7	13.1	14.3	8.52	15.7	12.5	11.0
Nd	35.9	52.4	51.9	58.5	36.2	64.1	51.4	45.3
Sm	6.84	9.94	9.17	11.0	6.96	12.0	9.66	8.35
Eu	2.12	3.01	2.73	3.3	2.13	3.58	2.93	2.57
Gd	6.66	9.62	8.86	10.8	6.74	11.62	9.49	7.99
Tb	0.85	1.23	1.06	1.39	0.85	1.45	1.20	0.98
Dy	4.09	5.81	4.84	6.77	4.08	6.88	5.76	4.57
Ho	0.71	0.99	0.81	1.19	0.71	1.19	1.00	0.78
Er	1.91	2.54	2.12	3.21	1.89	3.12	2.67	2.06
Tm	0.23	0.29	0.24	0.39	0.23	0.37	0.32	0.24
Yb	1.36	1.71	1.41	2.37	1.34	2.16	1.93	1.43
Lu	0.18	0.22	0.18	0.32	0.18	0.29	0.26	0.19

Table 2

Table 2

	MI					Gl	
Rock type	Picrite				Basalt	Picrite	
n. av. an.	*2*	*1*	*1*	*3*	*1*	*1*	4
sample	LAL70 * (Ol -16%, Fo 87)	LAL73-a	LAL73-b	LAL73-c	LAL42	LAL73-d	LAL73-e
SiO_2 *(wt%)*	43.46	47.00	51.09	52.06	52.36	52.45	55.55
TiO_2	3.12	3.36	5.37	4.48	4.03	2.55	2.22
Al_2O_3	10.87	11.08	12.80	14.33	15.01	16.10	17.97
FeO_{Tot}	15.66	9.96	6.90	7.80	7.81	10.13	6.86
MnO	0.08	0.13	0.07	0.14	0.13	0.21	0.15
MgO	15.42	7.44	5.89	3.33	3.32	1.89	1.13
CaO	8.04	13.76	14.99	14.71	13.28	6.74	4.84
Na_2O	1.94	1.55	1.61	2.72	2.81	2.78	4.38
K_2O	0.72	1.15	1.48	1.31	1.46	1.64	2.02
P_2O_5	0.50	0.51	0.58	0.83	0.66	0.81	0.95
Cr_2O_3	0.12	0.15	-	-	-	0.02	0.04
NiO	-	0.09	0.25	0.01	0.03	-	-
F	-	0.18	0.22	0.10	0.00	0.16	0.27
Cl	-	0.00	0.03	0.06	0.03	0.05	0.07
Tot	99.93	96.36	101.27	101.88	100.92	95.53	96.44
mg#	0.61	0.60	0.63	0.46	0.46	0.27	0.24
n. av. an.	*1*		*2*		*1*	*2*	
Sr *(ppm)*	558		883		838	1178	
Y	19.7		29.9		37.3	36.7	
Zr	202		289		386	458	
Hf	4.71		9.80		9.78	10.55	
Nb	35.2		53.2		43.7	84.3	
Ta	1.53		2.46		2.63	4.87	
La	24.3		38.8		43.6	69.6	
Ce	53.7		89.0		97.0	144.3	
Pr	6.92		10.6		12.72	16.37	
Nd	34.3		45.6		56.6	71.2	
Sm	7.92		10.8		12.84	15.86	
Eu	2.48		3.93		3.83	4.61	
Gd	5.84		9.38		11.14	11.10	
Tb	0.82		1.53		1.76	1.71	
Dy	5.16		7.23		8.40	8.38	
Ho	0.98		1.19		1.60	1.54	
Er	1.90		2.31		3.55	2.79	
Tm	0.20		0.21		0.45	0.52	
Yb	1.39		1.63		3.78	3.37	
Lu	0.18		0.24		0.36	0.44	
Th	1.61		2.78		4.55	8.05	
U	0.43		0.98		1.63	3.03	

* corrected for reheating simulation (after Danyushevsky, 2012)

Table 3

	Ethiopian Plateau (Lalibela suite)																			Yemeni Plateau (Manakhah suite)		
Rock type	Picrite							Basalt												Basalt		
sample	LAL41		LAL45		LAL70	LAL73		LAL31		LAL 42		LAL43		LAL44		LAL65		LAL69		YE28		
Cpx crystal n.	1	5	2	5	3	5	3	2	4	1-2	5	1	2	1	2	2	4	3	4	1	2	3
n. av. an.	2	2	2	2	3	3	2	3	4	3	6	4	2	2	2	2	2	3	2	4	3	3
Rb *(ppm)*	0.01	0.01	0.01	0.02	0.47	0.00	0.00	0.01	1.54	0.04	0.11	0.01	0.02	0.01	0.01	0.40	0.17	0.12	0.03	0.01	0.02	0.02
Sr	40.4	35.1	58.7	75.6	66.6	57.9	81.6	52.1	52.8	48.2	48.0	69.2	65.9	69.0	56.6	85.8	87.5	86.8	75.2	117	109	92.1
Ti	6978	4062	6864	10012	9374	7632	7260	7400	5634	7398	7389	7494	8153	7128	5015	12083	9733	10869	8981	11286	11271	10231
Y	9.20	5.13	8.70	13.7	16.8	9.16	7.45	14.3	8.67	13.4	11.4	8.60	8.06	7.82	3.69	19.09	19.17	16.1	12.9	24.1	18.2	13.8
Zr	20.8	7.11	21.3	50.5	49.4	30.0	22.9	34.5	28.6	30.1	28.4	23.5	23.9	19.5	7.06	70.71	63.84	66.5	45.4	125	86.3	70.7
Hf	1.10	0.37	1.18	2.46	2.17	1.74	0.92	1.67	1.11	1.33	1.31	1.26	1.06	1.19	0.28	3.39	2.91	3.45	2.29	5.20	3.82	3.28
Nb	0.06	0.01	0.09	0.21	0.32	0.29	0.39	0.15	0.28	0.41	0.10	0.07	0.20	0.07	0.03	0.31	0.26	0.31	0.13	0.96	0.59	0.43
Ta	0.01	0.00	0.01	0.03	0.02	0.01	0.02	0.01	0.03	0.02	0.01	0.01	0.00	0.01	0.00	0.05	0.03	0.04	0.01	0.17	0.11	0.08
La	1.24	0.71	1.71	3.26	3.41	2.20	2.02	2.08	2.43	1.96	1.82	1.68	1.68	1.47	0.79	3.73	3.36	3.93	2.97	11.4	5.94	5.56
Ce	5.19	3.21	7.41	13.2	13.8	7.56	7.77	10.3	7.17	7.89	8.06	7.91	8.13	6.24	4.14	15.14	14.48	16.7	11.9	43.6	25.2	22.4
Pr	1.13	0.64	1.37	2.44	2.67	1.53	1.30	2.08	1.18	1.46	1.49	1.58	1.52	1.34	0.75	3.04	2.86	3.12	2.40	7.54	4.43	3.82
Nd	6.90	4.04	8.2	13.9	17.6	7.89	7.79	11.0	6.83	10.4	9.79	8.64	9.63	8.11	4.43	18.7	18.0	19.1	14.5	39.5	25.7	20.2
Sm	2.41	1.70	2.85	5.18	4.82	3.12	2.42	4.05	2.32	4.24	3.03	3.34	4.10	2.94	1.91	6.13	5.99	5.86	4.54	10.1	6.85	5.70
Eu	0.85	0.54	1.05	1.51	1.62	0.83	0.88	1.37	0.72	1.13	1.22	1.16	1.17	0.92	0.57	2.21	2.05	2.09	1.58	3.16	2.57	1.84
Gd	2.72	1.64	2.82	4.15	4.98	2.70	2.63	4.22	2.34	3.87	2.96	3.06	3.23	2.32	1.46	5.74	6.15	5.61	4.10	8.26	5.72	4.51
Tb	0.40	0.22	0.43	0.63	0.73	0.39	0.35	0.71	0.34	0.55	0.47	0.44	0.43	0.36	0.24	0.86	0.93	0.79	0.59	1.16	0.92	0.66
Dy	2.42	1.48	2.16	3.30	4.42	2.10	2.08	3.80	1.99	3.41	2.78	2.02	2.28	2.12	1.22	5.01	4.89	3.75	3.42	6.21	5.03	3.43
Ho	0.39	0.24	0.38	0.60	0.78	0.41	0.29	0.70	0.38	0.55	0.49	0.37	0.39	0.33	0.19	0.80	0.83	0.67	0.50	1.04	0.78	0.58
Er	0.80	0.69	0.88	1.35	1.40	0.59	0.68	1.49	0.83	1.42	0.98	0.75	0.90	0.78	0.29	1.91	1.90	1.59	1.20	2.74	1.80	1.39
Tm	0.11	0.07	0.10	0.16	0.20	0.06	0.11	0.18	0.10	0.16	0.13	0.10	0.12	0.07	0.03	0.18	0.20	0.15	0.15	0.32	0.22	0.17
Yb	0.73	0.36	0.70	0.81	1.27	0.48	0.55	1.01	0.67	1.19	0.96	0.60	0.59	0.32	0.20	1.26	1.41	1.15	0.97	1.84	1.48	1.08
Lu	0.08	0.05	0.07	0.11	0.19	0.05	0.07	0.14	0.07	0.12	0.12	0.09	0.10	0.06	0.03	0.15	0.14	0.11	0.12	0.23	0.20	0.11
Th	0.01	0.01	0.01	0.02	0.08	0.03	0.01	0.01	0.32	0.09	0.03	0.01	0.09	0.01	0.00	0.04	0.03	0.02	0.01	0.10	0.03	0.03
U	0.00	0.00	0.00	0.00	0.02	0.01	0.02	0.00	0.23	0.03	0.02	0.00	0.01	0.00	0.00	0.01	0.01	0.01	0.00	0.01	0.00	0.01
Pb	0.04	0.17	0.09	0.07	0.17	0.18	0.25	0.19	4.91	0.19	0.52	0.16	0.14	0.13	0.22	0.03	0.12	0.09	0.04	0.14	0.09	0.10

Table 4

Affinity	sample		$^{87}Sr/^{86}Sr$	$^{87}Sr/^{86}Sr_i$	$^{143}Nd/^{144}Nd$	$^{143}Nd/^{144}Nd_i$	$^{206}Pb/^{204}Pb$	$^{206}Pb/^{204}Pb_i$	$^{207}Pb/^{204}Pb$	$^{207}Pb/^{204}Pb_i$	$^{208}Pb/^{204}Pb$	$^{208}Pb/^{204}Pb_i$
Ethiopian Plateau												
LT-Bas	SIM15	Bulk Rock	0.70367	0.70367	0.51288	0.51285	18.44	18.42	15.55	15.55	37.91	37.89
LT-Bas	SIM17	Bulk Rock	0.70373	0.70373	0.51280	0.51277	18.22	18.19	15.53	15.53	37.67	37.63
LT-Bas	ADG3	Bulk Rock	0.70329	0.70329	0.51306	0.51303	18.31	18.30	15.51	15.51	37.97	37.95
LT-Bas	ADG6	Bulk Rock	0.70320	0.70320	0.51298	0.51295	18.32	18.30	15.52	15.52	37.92	37.91
HT1-Bas	LAL32	Bulk Rock	0.70368	0.70366	0.51302	0.51300	18.71	18.63	15.56	15.56	38.50	38.45
HT1-Bas	LAL77	Bulk Rock	0.70412	0.70408	0.51289	0.51286	18.59	18.48	15.52	15.52	38.13	38.05
HT1-Bas	BLN2	Bulk Rock	0.70429	0.70428	0.51292	0.51290	18.86	18.79	15.59	15.59	38.47	38.39
HT1-Bas	BLN4	Bulk Rock	0.70371	0.70369	0.51294	0.51291	18.57	18.51	15.51	15.51	38.37	38.29
HT2-Bas	LAL14	Bulk Rock	0.70424	0.70420	0.51295	0.51293	19.26	19.11	15.56	15.55	38.76	38.58
HT2-Bas	LAL31	Bulk Rock	0.70415	0.70408	0.51299	0.51296	18.95	18.72	15.58	15.57	38.76	38.58
HT2-Bas	LAL42	Bulk Rock	0.70437	0.70432	0.51296	0.51293	18.96	18.77	15.57	15.56	38.41	38.27
		Cpx	0.70436	0.70436	0.51299	0.51294	18.83	18.81	15.59	15.59	38.45	38.43
HT2-Bas	LAL43	Bulk Rock	0.70406	0.70402	0.51303	0.51300	19.12	18.92	15.59	15.58	38.93	38.72
HT2-Bas	LAL44	Bulk Rock	0.70417	0.70412	0.51295	0.51292	19.02	18.84	15.55	15.54	38.87	38.72
		Cpx	0.70467	0.70412	0.51300	0.51295	18.45	18.45	15.40	15.40	38.23	38.23
HT2-Bas	LAL65	Bulk Rock	0.70433	0.70427	0.51301	0.51299	19.03	18.90	15.58	15.57	38.96	38.87
		Cpx	0.70429	0.70429	0.51301	0.51297	18.81	18.77	15.60	15.60	38.77	38.73
HT2-Bas	LAL68	Bulk Rock	0.70418	0.70415	0.51294	0.51291	19.07	18.88	15.58	15.57	38.96	38.82
HT2-Bas	LAL69	Bulk Rock	0.70412	0.70404	0.51302	0.51230	19.08	18.97	15.58	15.58	39.13	39.04
		Cpx	0.70412	0.70412	0.51303	0.51299	18.96	18.94	15.64	15.64	39.06	39.04
HT2-Pi	LAL33	Bulk Rock	0.70409	0.70405	0.51300	0.51297	18.94	18.82	15.56	15.55	38.71	38.61
HT2-Pi	LAL41	Bulk Rock	0.70417	0.70408	0.51296	0.51294	18.95	18.83	15.59	15.58	38.76	38.65
HT2-Pi	LAL45	Bulk Rock	0.70401	0.70394	0.51298	0.51296	19.05	18.93	15.58	15.58	39.13	38.72
HT2-Pi	LAL47	Bulk Rock	0.70418	0.70412	0.51296	0.51293	19.08	18.97	15.58	15.58	38.84	38.76
HT2-Pi	LAL70	Bulk Rock	0.70404	0.70399	0.51290	0.51288	19.07	18.97	15.63	15.63	38.99	38.93
		Cpx	0.70454	0.70453	0.51297	0.51294	18.51	18.48	15.43	15.42	38.30	38.26
HT2-Pi	LAL73	Bulk Rock	0.70414	0.70407	0.51294	0.51292	18.99	18.88	15.55	15.55	38.89	38.83
		Cpx	0.70439	0.70439	0.51301	0.51297	18.61	18.59	15.54	15.54	38.56	38.55
Yemeni Plateau												
HT2-Bas	YE23	Bulk Rock	0.70363	0.70363	0.51290	0.51290	19.41	19.24	15.61	15.60	39.46	39.29
HT2-Bas	YE24	Bulk Rock	0.70359	0.70358	0.51299	0.51297	18.91	18.74	15.55	15.54	38.89	38.71
HT2-Bas	YE25	Bulk Rock	0.70362	0.70362	0.51290	0.51288	19.22	19.13	15.55	15.55	39.21	39.12
HT2-Bas	YE27	Bulk Rock	0.70371	0.70368	0.51288	0.51285	19.26	19.07	15.55	15.54	39.26	39.04
HT2-Bas	YE28	Bulk Rock	0.70370	0.70368	0.51289	0.51287	18.96	18.81	15.57	15.56	39.01	38.84
HT2-Bas	YE31	Bulk Rock	0.70368	0.70365	0.51293	0.51291	19.38	19.26	15.61	15.61	39.39	39.26
HT2-Pi	YE26	Bulk Rock	0.70372	0.70371	0.51289	0.51287	19.00	18.89	15.60	15.60	39.13	39.01
HT2-Pi	YE29	Bulk Rock	0.70367	0.70362	0.51295	0.51293	19.00	18.85	15.57	15.56	38.95	38.80

Table 5

Affinity	sample	$^{3}He/^{4}He$ (R/R_A)		
Ethiopian Plateau				
HT2-Bas	LAL31	17.8	±	0.7
HT2-Bas	LAL42	12.9	±	0.7
HT2-Bas	LAL43	19.1	±	1.3
HT2-Bas	LAL44	15.6	±	0.4
HT2-Pi	LAL6	10.4	±	0.9
HT2-Pi	LAL11	10.6	±	0.6
HT2-Pi	LAL33	15.7	±	1.0
HT2-Pi	LAL41	16.8	±	0.5
HT2-Pi	LAL47	18.3	±	0.6
HT2-Pi	LAL70	3.7	±	0.8
HT2-Pi	LAL73	9.6	±	1.0

Table 6

Affinity	sample	mineral	$\delta^{18}O$ (‰)		
Ethiopian Plateau					
HT2-Bas	LAL42	Olivine	6.12	±	0.08
HT2-Bas	LAL42	Cpx	5.82	±	0.09
HT2-Bas	LAL70	Olivine	5.21	±	0.17
HT2-Bas	LAL70	Cpx	5.82	±	0.22
HT2-Pi	LAL73	Olivine	6.62	±	0.21
HT2-Pi	LAL11	Cpx	6.90	±	0.08